DEVELOPMENT OF A POSITION SENSITIVE ENERGY-DISCRIMINATING - (PSED) - DETECTOR FOR X-RAY DIFFRACTION

FINAL REPORT

itres RESEARCH LIMITED

DEVELOPMENT OF A POSITION SENSITIVE ENERGY-DISCRIMINATING - (PSED) - DETECTOR FOR X-RAY DIFFRACTION

FINAL REPORT

BY

ITRES Research Limited
#110 - 6815 8th St. N.E.
Calgary, Alberta
T2E 7H7

October 1, 1988

Work on this report was conducted under the auspices of the Department of Energy, Mines & Resources.

DSS File Number:	075Q.23440-7-9152
DSS Contract Number:	233440-7-9152/01SQ
EMR Scientific Authority:	Dr. R. Packwood

70 pp

MICROMEDIA

TABLE OF CONTENTS

I Executive Summary 1

II Introduction 2

III Technical Discussion 3

1) Background 3

2) System Upgrade 6
a) Electronics 6
b) Chamber 7
c) Software 8

3) X-Ray Detection Tests - Results & Analysis 9
a) Preparation 9
b) Standard CCD X-ray Tests 11
c) High Resistivity CCD X-ray Tests 13
d) Detection Efficiency Analysis 15

IV Conclusions 23

V Appendix A 27

Discussions On Key Factors Affecting The Performance of CCD's As Detectors Of Low Energy X-rays.

VI Appendix B - Related Scientific Papers 40

1) Lumb et al. "X-ray Measurements Of Charge Diffusion Effects In EEV Ltd. Charge-Coupled Devices"

2) Janesick et al. "Charge-Coupled Device Advances X-ray Scientific Applications In 1986"

I Executive Summary

Experimentation to determine the capability of the EEV Standard (P86223) CCD (3 µm depletion region) and the experimental EEV High Resistivity (P8600HR) CCD (30 µm depletion region) has been successfully completed. System characteristics such as system noise and charge transfer efficiency (CTE) were analyzed and the system modified to optimize it for the detection of x-rays. Once the system performance had been pushed close to its limits, x-ray tests were performed.

The analysis of the data provided results much improved over previous ITRES tests. Collection of the x-ray induced charge on the CCD was accomplished with reduced charge smearing due to improved CTE. X-ray events became much more resolvable from the background levels for this reason as well as lower system noise levels. The performance of the standard CCD proved to be significantly better than anticipated. Results from the P8600HR X-Ray CCD test data were expected to show considerable improvement over the standard CCD tests. The extent of these expected improvements were not fully realized due to a problem linked to the output transistor of the experimental device supplied to us. The data did suggest, however, that a properly functioning high resistivity device should produce superior data to that obtained with the standard EEV CCD.

II Introduction

During the past few years, ITRES Research Limited has had a strong belief that Charge Couple Devices (CCDs) could be used to create a detector useful for general x-ray diffraction applications. Initial experimentation had been completed by ITRES in this field with its work for CANMET on the development of a position sensitive x-ray detector based on CCD technology. Due to constraints imposed by this specific application, the results were not immediately applicable. However, they were sufficiently encouraging to persuade ITRES of the value of following up the project with a program to determine the feasibility of using CCD's detectors in various x-ray applications.

In order to create a system that would adequately discriminate x-ray energy levels, it was recognized that improvements would be needed in two areas. Firstly, the noise level of the CCD readout system needed to be minimized. Secondly, the ability of the CCD itself to fully collect the x-ray produced charge needed to be improved. The first of these could be done in-house by painstaking work on ITRES's Test Facility System electronics. The latter improvement would be accomplished in two different ways, by optimizing the Test System's readout mechanisms and by optimizing the CCD itself. Fortunately, some work has been ongoing on improving the CCD design for x-ray imagery applications by EEV, and an experimental x-ray device was obtained for testing purposes. On the improved test system, both a standard CCD and the experimental x-ray device were tested for their ability to collect and discriminate x-ray events. This report summarizes the efforts made to improve the test system and the results of the consequent x-ray testing and analysis.

III Technical Discussion

1) Background

In the previous work ITRES has performed on the utilization of CCD's as x-ray sensors, many of the shortcomings of ITRES's test facility became apparent. The system achieved a noise floor of 166e-. The system was set up so that each 70 electrons of CCD signal are converted to 1 digital number (dn). (ie: quantizing step size = 1/system gain = 70 e-/DN). Each x-ray event in the 1-10 kev range, captured in the silicon CCD structure, is expected to produce 1 electron for each 3.65 ev of x-ray energy. Tests were performed using 5.9 Kev x-rays produced by a Fe 55 source. A total of 1620 electrons are therefore expected to be produced for each x-ray absorption. A histogram of the data was expected to produce x-ray peaks at 23 dn intervals, but the observed standard deviation was greater than one tenth the size of the x-ray peak separation. With such a large noise component, it became difficult to distinguish between the effects of the noise and the effects of charge spreading or charge smearing on the CCD itself. This factor needed to be reduced for this reason as well as for the future needs of achieving better energy resolution.

Another problem that compromised analysis in the previous x-ray project was that of data integrity due to problems on the CCD. The device used in that testing, although appearing defect free in most respects, apparently had some column defects related to the Horizontal Transport Register (HTR). A question that was never fully resolved related to the effect of the HTR defect on data transferred through that defective pixel. Any subsequent testing, it was

decided, should take place on a CCD which was, as much as possible, free from defects, with particular attention being given to HTR defects.

Reduced noise levels make it possible to better analyze the data to check for other potential problems. Although Charge Transfer Efficiency (CTE) was tested in the previous work, a much better analysis could now be performed, allowing us more fully to optimize the system.

Despite the less-than-optimal noise performance achieved by the old version of the Test Facility, it was still clear that the energy resolving capabilities of the system were compromised by the effects of charge spreading in the field free region of the CCD. Since then experimental work has been carried out by EEV to produce a device that is optimized for x-ray detection. To date, their efforts to accomplish this goal have met with some success, the objective being to produce an x-ray-optimized CCD by maximizing the depleted region of the CCD while at the same time minimizing the depth of the field free region of the epitaxial layer on which the CCD is created. This is accomplished by utilizing a special high resistivity wafer on which to produce this device.

The production of this material is much more difficult than the production of the material used in the standard device. The quality of the high resistivity material used for device fabrication is generally poorer than that of the standard resistivity material. At present an experimental device has been made available to ITRES for testing purposes. Other higher grade - high resistivity devices were produced by EEV, which apparently performed very well, but these are not available to ITRES at this time. A more complete explanation of the

EEV X-ray enhanced CCD is given later in the paper as well as in Appendix A.

When this project was first proposed, it was to be of large enough proportions to complete the groundwork to design a Position Sensitive Energy Discriminating (PSED) X-Ray detector for use in diffractometry systems.

The system specifications at that time were to be the following:

Energy Resolution	.5 KeV
	133 e-
Readout Noise	20 - 30 e-
Readout Rate	1 - 10 microseconds/pixel
Quantizing Step Size	10 - 20 e- /DN
Digitizing Range	10 - 12 bits
CCD Temperature	- 55 to - 70°C
Dark Current	10 - 20 e- /sec/pixel or
	50 - 100 e- /sec/pixel with hardware or software compensation

In the scaled down project that was finally launched to provide test results to aid in determining the fully exploited x-ray capabilities of CCD's, it was necessary to compromise on some of these specifications. Nevertheless, these specifications continued to represent our aspirations for the upgraded system, except that we hoped to be able to avoid the need for cryogenic cooling of the CCD.

2) System Upgrade

a) Electronics

A new Analogue Signal Chain (ASC) was to be implemented into the test system for use during the x-ray experimental phase of the project. The design, to have lower noise levels as well as lower power consumption than with the previous version of the ASC, while maintaining a high speed readout rate, was based on a proven design supplied by the Jet Propulsion Laboratory in California. The ASC was to operate at 1 megapixel/second, roughly the maximum speed at which ITRES Test Facility is capable of reading out the CCD.

Unfortunately many problems were encountered with the design. A considerable amount of effort was required to get the ASC working in an acceptable manner. Although solutions were eventually found for all the problems, some compromises were made in order to have the system working in time to complete the project.

The ASC was capable of operating only at ≈ .4 Megapixel/second, not at the 1 megapixel/sec rate that the design indicated. A Background Level Subtraction (BLS) capability was included in the design so that the electronic background could be removed in real time. This feature would have allowed the system to provide more consistent data for analysis. However, it was not performing properly and was not available during the testing period.

The system noise of the new test facility was considerably improved over the old system. With considerable effort made to optimize the system grounding

and shielding, the new system yielded a consistent noise floor of 60-70e-, almost three times less than was achieved on the old system. It is still much higher than the final objective of 20-30e-. Some additional improvement in the readout noise may be obtained when all the problems with the ASC design are corrected. More likely, improvements could be made on the noise at this point by work on the preamp circuit. This is also related to the fact that the objective for the quantizing step size was not met. A value of 60e-/dn was achieved as opposed to the desired 10-20e-/dn. Pushing this factor any lower by changing gain stages on either the ASC or preamp boards, started to degrade the wave form to be digitized.

As can be seen in the above discussion, the ultimate specifications as listed in the Background Section of the Technical Discussions, have not yet been met. However, significant improvements have been accomplished relative to the previous Test System.

b) Chamber

The new system configuration required that a new chamber be designed and fabricated. This new chamber was designed to be usable for as wide a variety of applications as possible. The primary consideration, however, was the incorporation of features required for the x-ray testing. These features included:

1) an electronic shutter between the CCD detector and the x-ray source, manually controllable from outside the chamber.

2) a moveable source to allow adjustment of the source to detector distance, manually adjustable from outside the chamber. The moveable source allows for the source-detector distance to be adjusted from 5.5 mm to 30.9 mm.

3) thermo-electric cooling of the CCD. For optimal cooling of this kind, careful design of the thermal system (cold finger, thermal electric device, heat sinking etc.) was required. As well, the chamber needed to be able to hold a purge of dry gas to eliminate the possibilities of condensation on the CCD once it was cooled. Temperatures of -17°C were achieved. This amount of cooling is significantly less than what was proposed in the original project. The designed -55 - -70 was not required for the tests and the development of a cryogenic cooling system that would have been required was out of the scope of the project.

c) Software

Most of the software utilized in this project was developed in-house to work hand-in-hand with the new ITRES Test Facility. Some routines had been developed for general system performance tests. Other routines were specifically designed for analysis of the x-ray data. The system performance software included functions to perform light transfer curves, charge transfer efficiency tests, as well as a program to display images of the CCD data. The main x-ray analysis program that was produced, known as XRAN, was developed in order to

produce histograms of the data stored on the test facility hardware or previously stored frames of data. The histograms, once produced, can be analyzed to produce statistics on either the entire, or any specified potion, of the histogram. As well the histogram can be plotted, scaled & labelled as the user desires. This program was then designed to dump the plot to a printer port. Unfortunately this feature could not be implemented due to hardware problems on the test facility. Another, somewhat slower method was implemented for producing a hardcopy of the histogram.

3) X-ray Detection Tests - Results & Analysis

a) Preparation

With the Test system working in an adequate fashion for standard imaging applications, the system was turned over to x-ray testing. Focused images were being displayed with a minimal amount of noise and data being collected for Light Transfer Curves (LTC) suggested a stable, well behaved system. A LTC is a standardized method of determining the performance capability of CCDs. The system is raised to various different uniform signal levels throughout its dynamic range. At each of these levels a measurement is made of the noise variance on the signal. The value is composed of three terms as indicated in the following equation:

$$\sigma^2 = A + B \cdot x + C \cdot x^2$$

where σ^2 = noise variance (dn^2)

A = read noise or noise floor (dn^2)

B = system gain (dn/e^-) ($B \cdot x$ = shot noise)

C = pixel to pixel variation coefficient

x = signal level (dn)

If the noise value that is measured is collected so as to eliminate pixel to pixel variations (C = 0), then a graph of σ^2 vs x will produce a straight line if the system is working in a proper manner. It can be shown that the term B, the slope of the before mentioned graph, is actually the gain of the entire system measured in digital numbers per photo-electron. This technique provides an overall system gain measurement which does not require knowledge of the electronic gain of the system or the CCD output gate capacitance.

When an image of the x-rays was produced, the events were found to be streaked over several horizontal pixels. If this problem was related to the expected charge spreading of the x-ray induced charge, the spreading would form a uniform spherical cloud and would not just spread horizontally. Hence the origin of this problem did not appear to be associated with charge spreading. An alternative explanation was that it could be a problem with poor Horizontal Charge Transfer Efficiency (CTE). Previous experience suggested that the CCD output gate voltage (V_{og}) level affects the CTE. When V_{og} was raised above the manufacturer's specified level, any evidence of CTE problems was eliminated. X-ray events now produce sharp point-like images. The system is now supplying the CCD with a non standard set of signals for optimal results. At present, the reason for this is unclear. Until it is known, the CTE should be checked with each change to the system, including the use of new CCDs.

The system now appeared to be ready for x-ray testing. A final LTC

characterization was done using the standard CCD. The system parameters derived from the LTC were:

- Quantizing Step size - 60 e-/dn

- Readout noise - 70 e-

At this quantizing step size we should expect to observe x-ray peaks, for the 5.9 kev x-rays, at intervals of

(5913 ev/x-ray) / (3.65 e-/ev) / (60 e-/dn) = 27 dn/x-ray

In the old test facility the peak separation was 10 times the noise floor (see Background section). In new system this factor has improved almost 2.5 times to 23.

b) **Standard CCD X-Ray Tests**

The actual x-ray testing started, as previously mentioned, with the collection of x-ray exposed frame images. The x-rays could clearly be seen as point-like objects superimposed on a uniform background. An observation of the event densities allowed an analysis of the uniformity of the x-ray flux. It was apparent that the flux rate was uniform throughout the image region of the CCD. Future tests that collected data from sub-areas of the array could be relatively independent of their location on the sensor.

A 100 X 100 pixel region near the centre of the array was chosen to provide data for analysis of x-ray events. Both a dark current frame and an x-ray frame were collected. The resultant data were used to create the histograms shown in Figures #1a and #1b by the program XRAN. Figure #1c shows the same data as Figure #1b, but scaled up. There is a clearly defined peak located 30 dn above the dark current peak suggesting a quantizing step size of (1600 e-/x-ray) / (30 dn/x-ray) = 53 e-/dn, not too different from the expected 60 e-/dn. With a standard deviation or noise level of 1.6 dn or approximately 100 e- for the dark current peak, and 105 e- noise for the x-ray peak, the two peaks should show up as fully isolated from one another if all of the charge produced by an x-ray was collected within the incident pixel. The large number of pixels which have collected a partial packet of x-ray charge showing up on the histogram in the gap between the two peaks, indicate that a large amount of charge spreading or splitting occurred when x-rays were absorbed in the field free region of the CCD. The 'tail' on the dark current peak, so easily observable in Figure #1c, suggests that many of the pixels are picking up a very small number of x-ray electrons, meaning that the spreading is likely occurring over several pixels. The rest of the plateau between the peaks is probable due to splitting of charge between a pair of pixels.

If the charge is spreading as it was believed, then one way of reducing the effects is to increase the area of the pixel. This, effectively can be accomplished by performing on-chip summation, a method by which the signal or charge found on adjacent pixels can be added together and read out as if they came from a single CCD element.

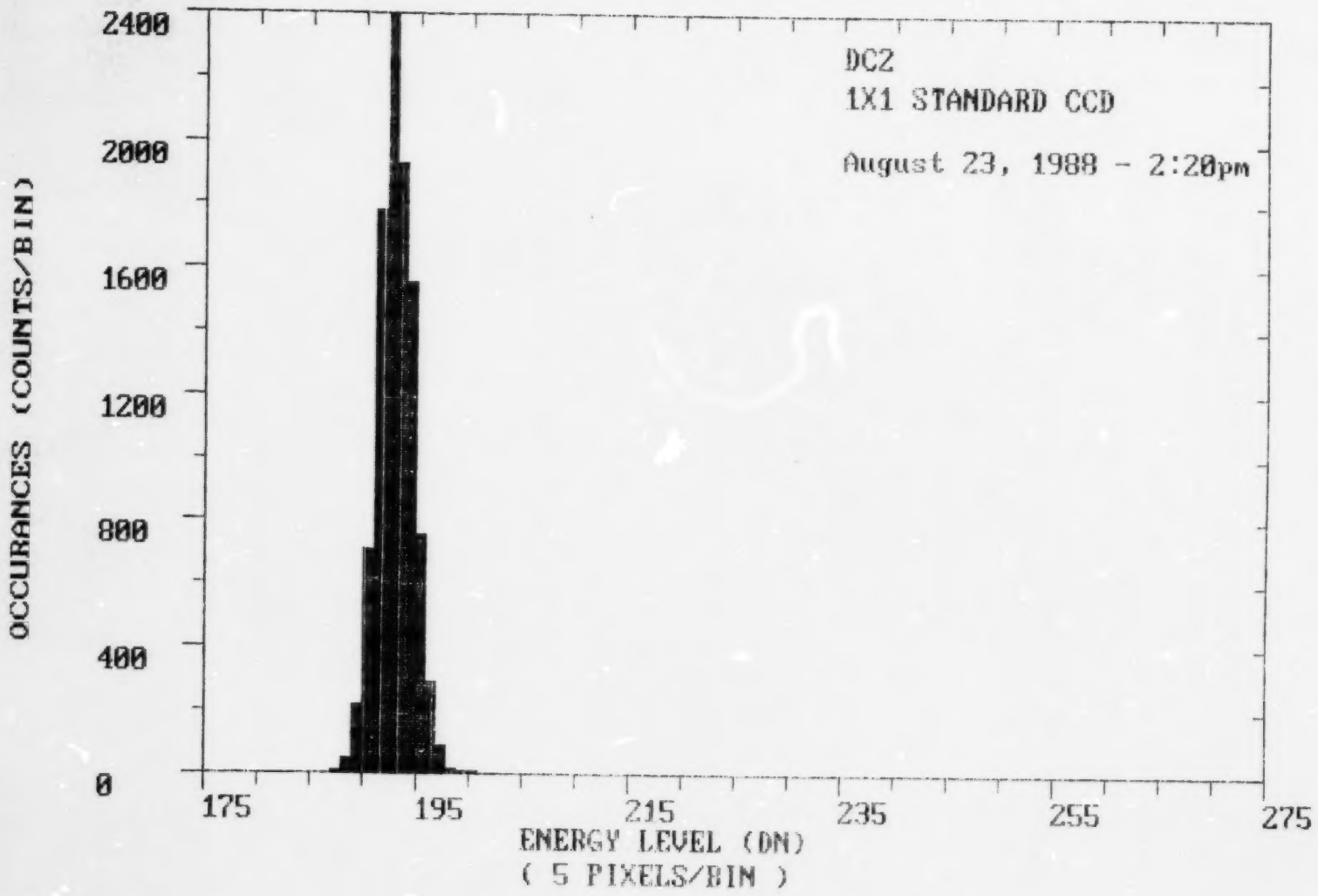
DC2
1X1 STANDARD CCD
August 23, 1988 - 2:20pm
OCCURANCES (COUNTS/BIN)
2400
2000
1600
1200
800
400
0
175
195
215
235
255
275
ENERGY LEVEL (DN)
(5 PIXELS/BIN)

FIGURE 1a

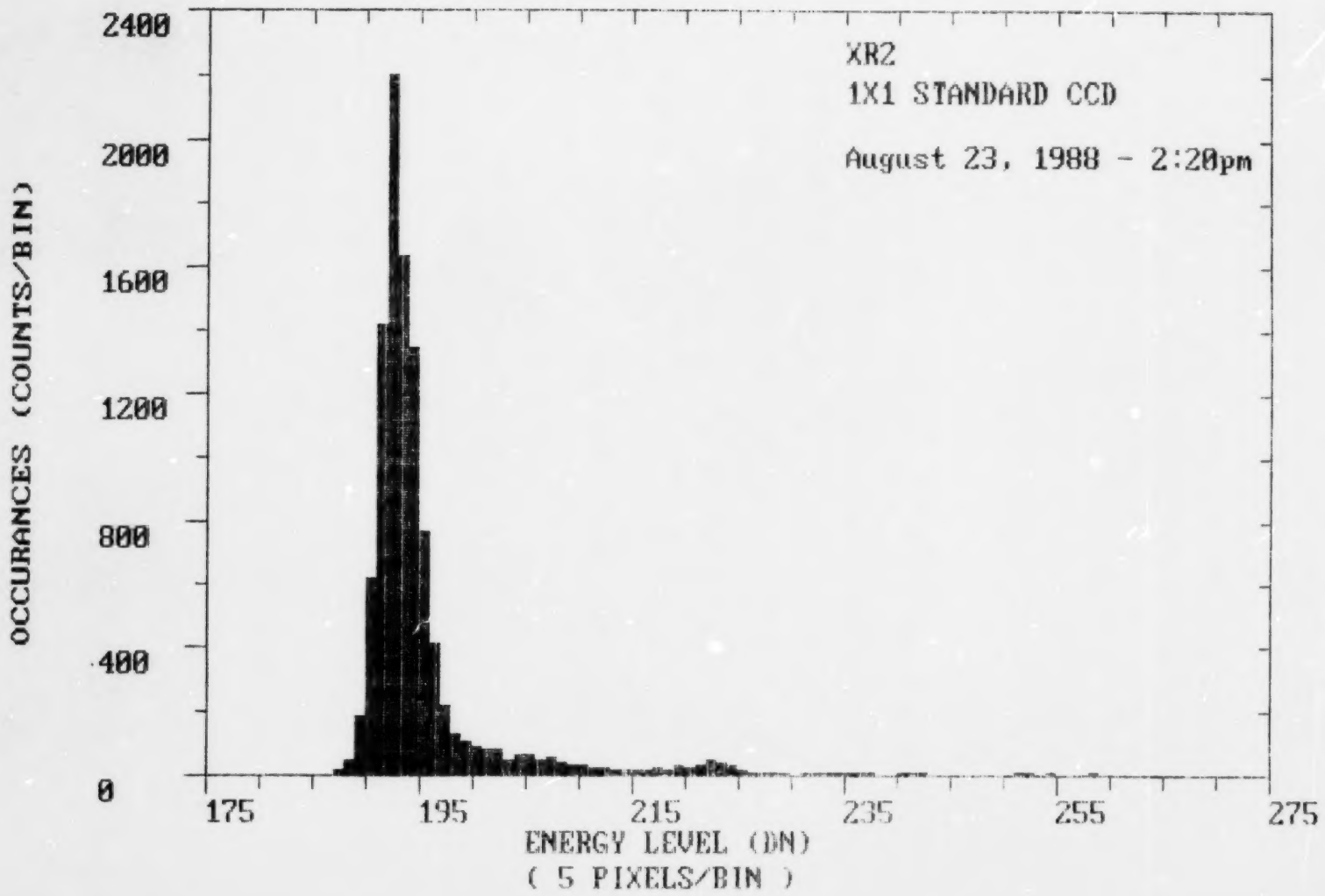
XR2
1X1 STANDARD CCD
August 23, 1988 - 2:20pm
OCCURANCES (COUNTS/BIN)
2400
2000
1600
1200
800
400
0
175
195
215
235
255
275
ENERGY LEVEL (DN)
(5 PIXELS/BIN)

FIGURE 1b

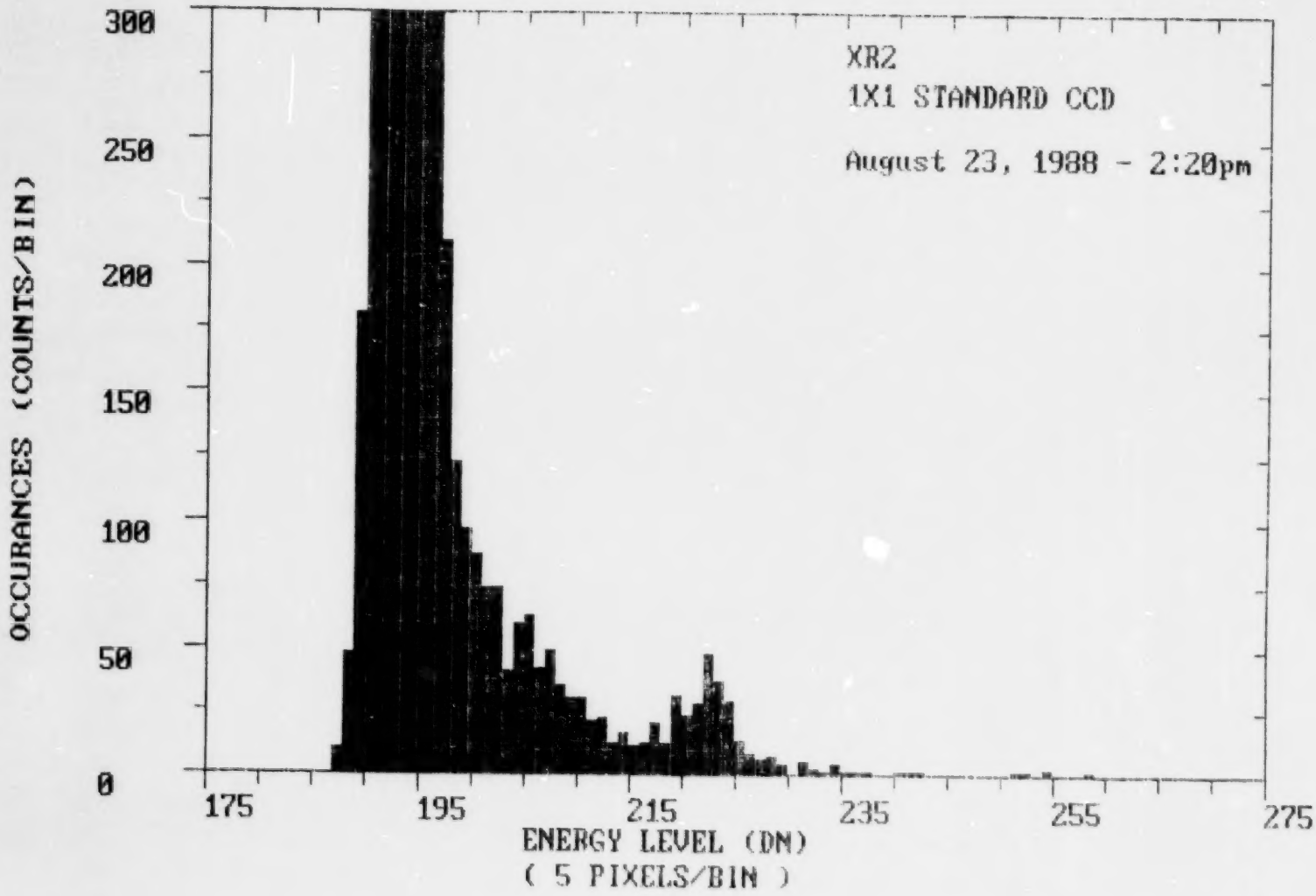
300
250
200
150
100
50
0
OCCURANCES (COUNTS/BIN)
XR2
1X1 STANDARD CCD
August 23, 1988 - 2:20pm
175
195
215
235
255
275
ENERGY LEVEL (DN)
(5 PIXELS/BIN)

FIGURE 1c

The histograms shown in the next three figures (#2a,b,c), is for 3 X 3 on-chip summation, but otherwise comparable to the 1 X 1 pixel data just examined. By summing the charge in the 9 pixels together, the noise performance of the system appears to be degraded, evident in the broader histogram of the dark frame data. The reason for this is not understood and needs further investigation. Fortunately the increased noise (up to 146 e- from 100 e-) is more than compensated for by the fact that the tail due to the extreme charge spreading is no longer noticeable. The space between the two peaks is now filled by a relatively flat plateau created by charge splitting between two adjacent pixels. As well the single x-ray peak has more counts in it than in the 1 X 1 case. A close look at the data shows 3 discernible x-ray peaks at 28 dn intervals which corresponding to single, double and triple x-ray event peaks. The 28 dn peaks indicates a quantizing step size of 57 e-/dn, very close to the LTC derived value of 60 e-/dn.

c) High Resistivity CCD X-ray Tests

Prior to an analysis of the HR-CCD x-ray data, several points about the setup of this CCD should be detailed. The experimental HR-CCD came in a larger package than the standard device, with 30 pins as opposed to 20. An adapter was therefore needed in order to drive the HR device. This board, will contribute an extra noise factor. As well, as indicated in the Appendix A, the quality of the wafer material used to manufacture the CCD is likely to be of poorer quality than that used in standard devices. If so, this may also contribute to higher noise levels.

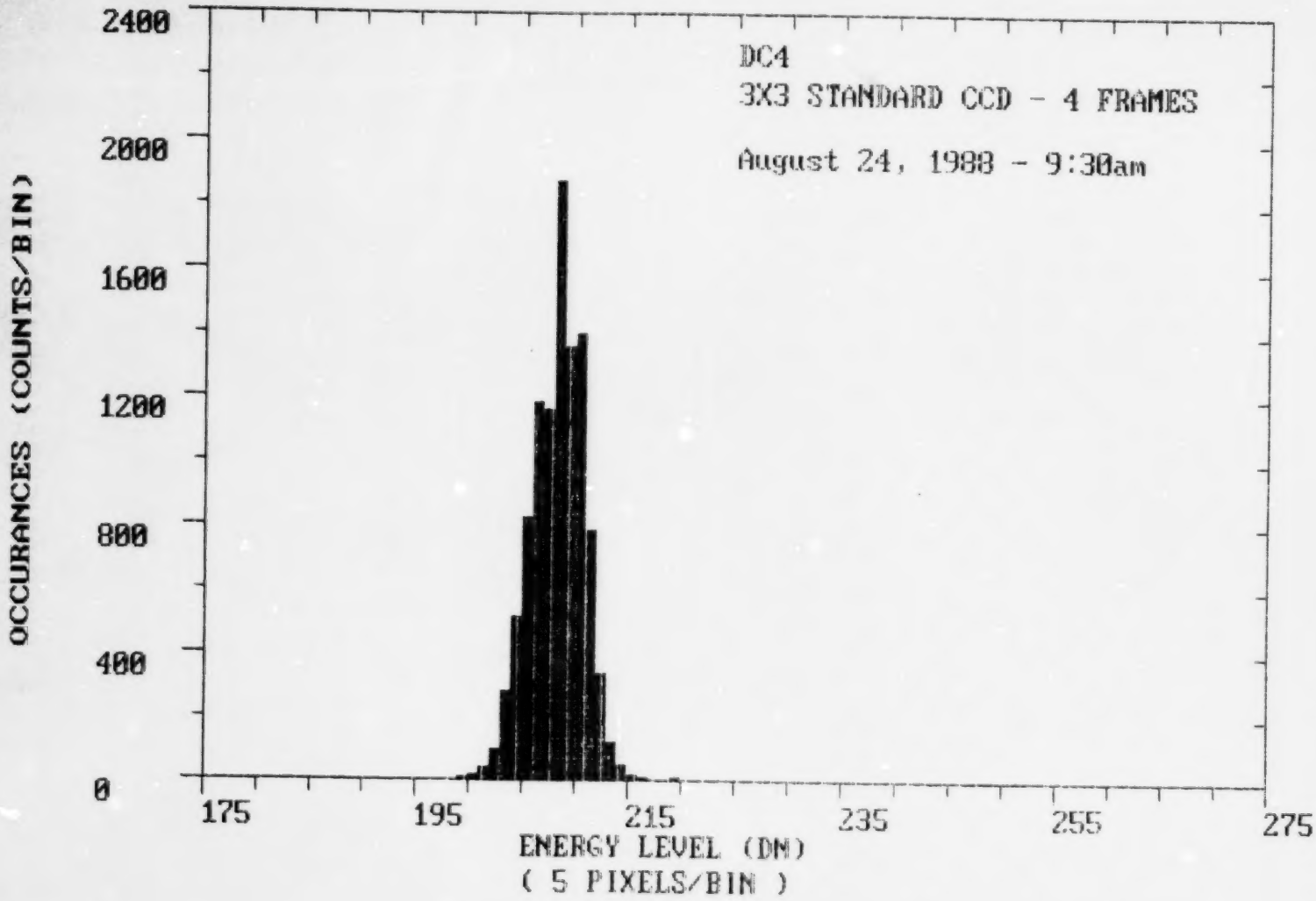
DC4
3X3 STANDARD CCD - 4 FRAMES
August 24, 1988 - 9:30am
OCCURANCES (COUNTS/BIN)
2400
2000
1600
1200
800
400
0
175
195
215
235
255
275
ENERGY LEVEL (DN)
(5 PIXELS/BIN)

FIGURE 2a

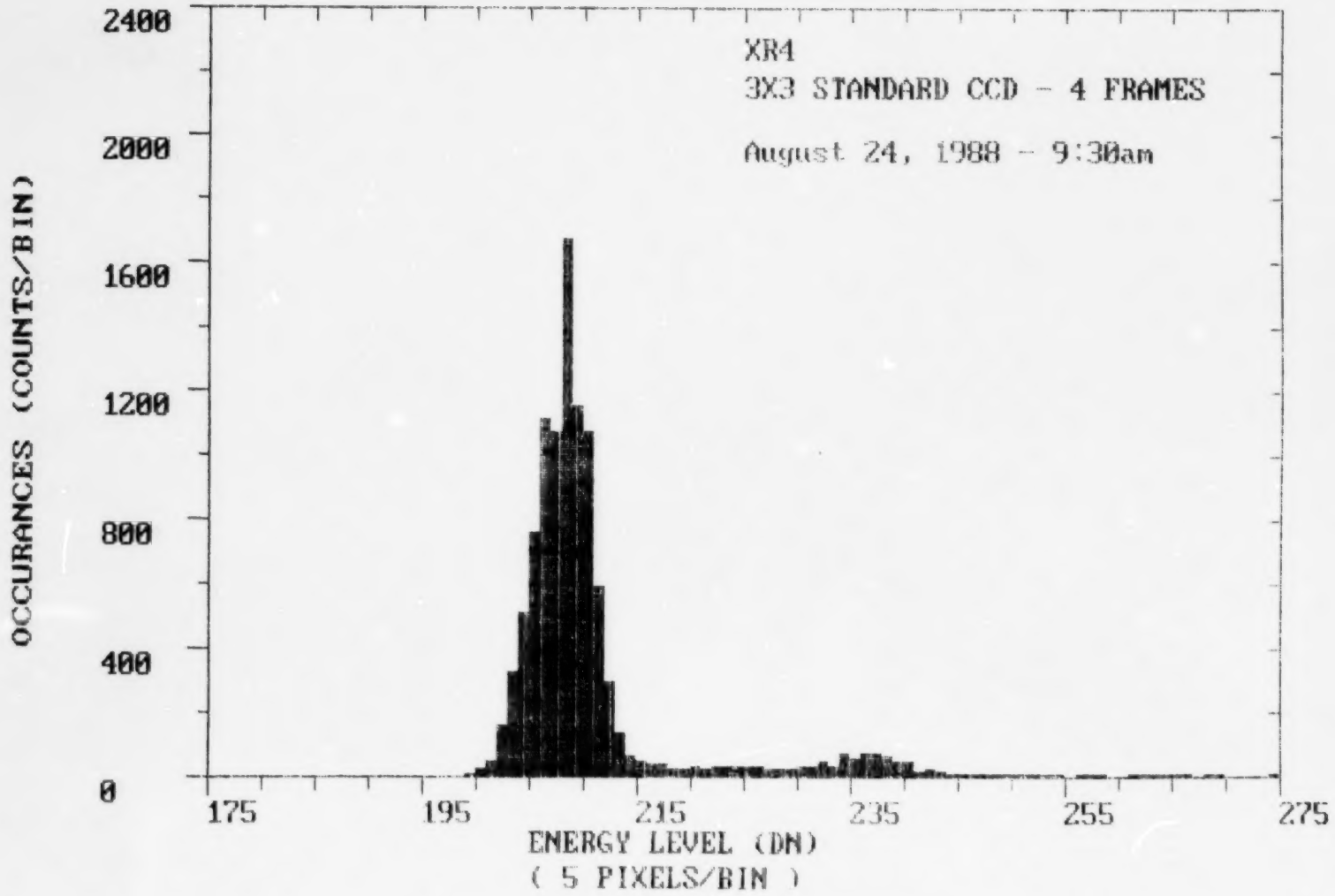
XR4
3X3 STANDARD CCD - 4 FRAMES
August 24, 1988 - 9:30am
OCCURANCES (COUNTS/BIN)
2400
2000
1600
1200
800
400
0
175
195
215
235
255
275
ENERGY LEVEL (DN)
(5 PIXELS/BIN)

FIGURE 2b

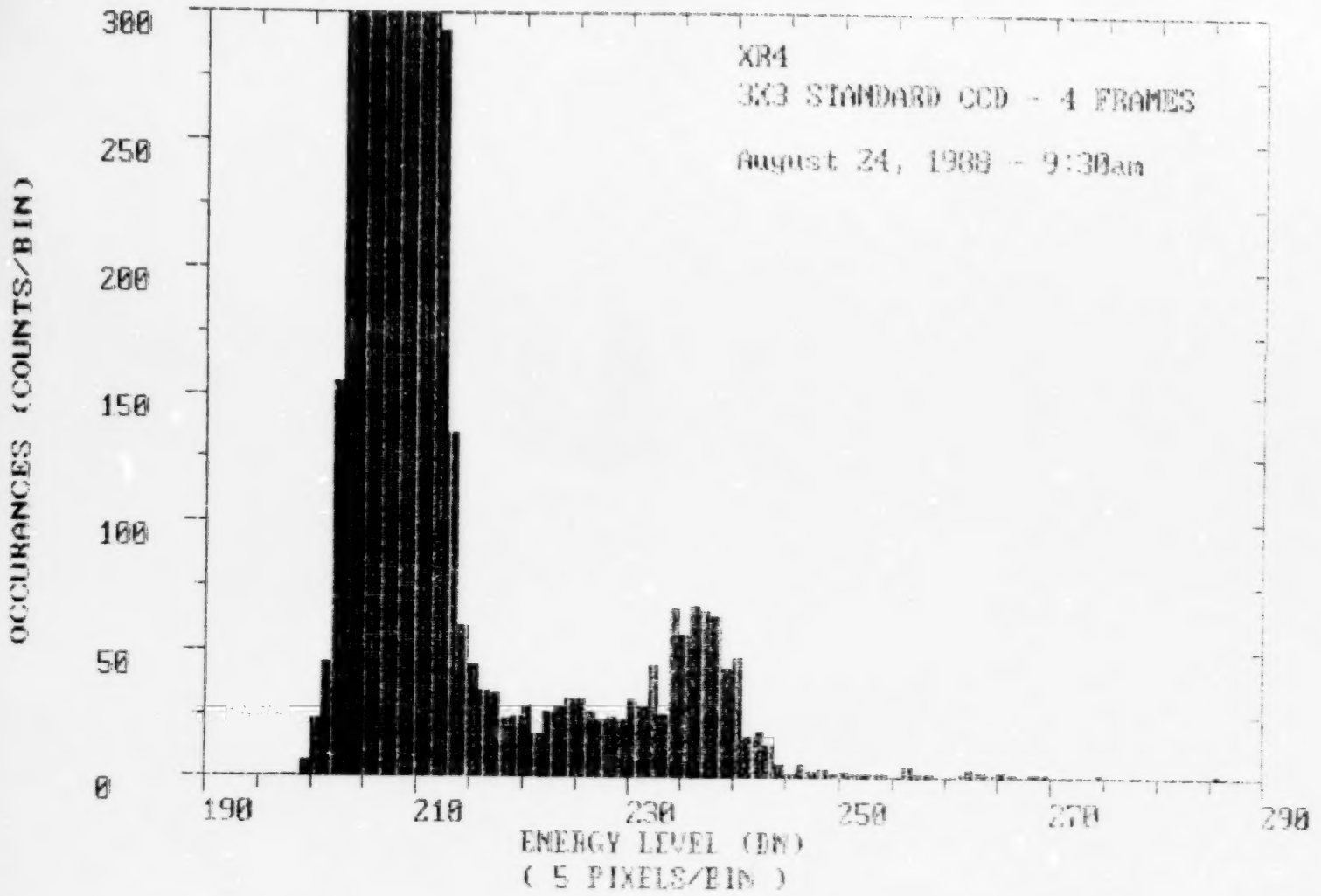
XR4
3X3 STANDARD CCD - 4 FRAMES
August 24, 1988 - 9:30am
OCCURANCES (COUNTS/BIN)
300
250
200
150
100
50
0
190
210
230
250
270
290
ENERGY LEVEL (DN)
(5 PIXELS/BIN)

FIGURE 2c

Upon initial operation of this device in x-ray tests, the resultant histogram showed the x-ray peak overlapping the dark current peak. The x-ray peak separation appeared only to be 10 dn rather than the expected 27 dn, implying an on-chip gain for this device which is several times smaller than for the standard device. The output transistor capacitance, which is related to the on-chip gain, should have a value between .15 & .20 pf (the high end of this range for the HR device). The measured capacitance of this device is nearly .70 pf, suggesting some defect in its output transistor. In order to work around this problem the gain needed to be adjusted. This was accomplished by adjusting the gain on the analogue signal chain. A LTC showed that the quantization step size was now at 52 e-/dn, a level similar to Standard CCD test step size and noise floor was now measured to be near 160 e-, up from the 70 e- determined for the standard device. This was expected as the increased gain also affected the noise levels. It should be noted that the gain of the ASC was now outside of the range that had previously been determined to provide the optimal signals to the Analogue to Digital converter.

X-ray data were then collected for the 1 X 1 case as shown in figures 3a,b,c. Although the width of the peaks are more than double the width of the standard CCD histograms, the separation of the dark current and single x-ray peaks appears to be superior. The 'tail' that appeared on the 1 X 1 standard CCD histogram is not apparent here, indicating that in the HR device fewer x-ray event electrons are spreading into more than two pixels. The probable reasons for this are discussed in the next section.

The data collected for the 3 x 3 pixel summation case gave extremely noisy data, with the dark current peak being twice as noisy as in the 1 x 1 case. (See

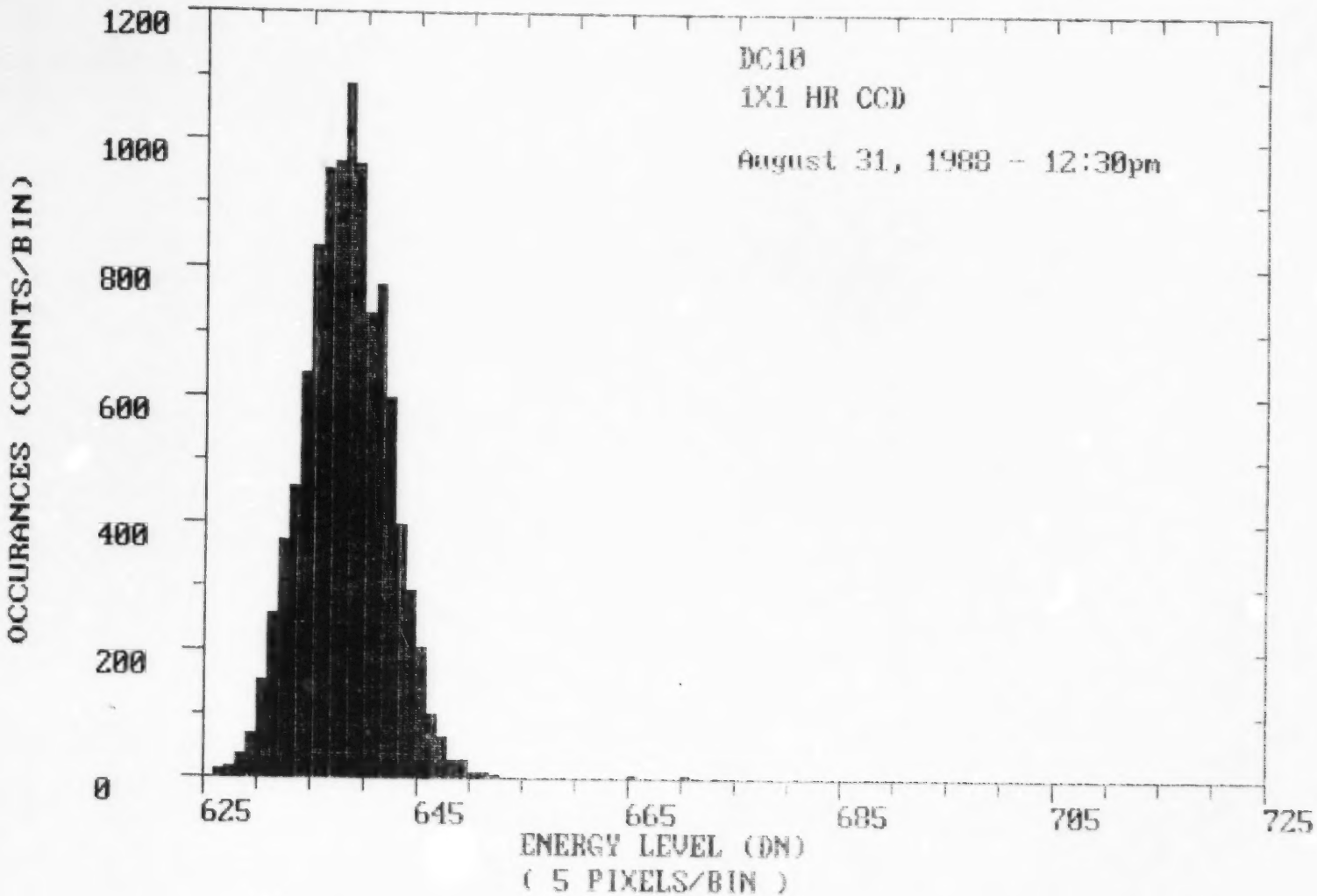
DC10
1X1 HR CCD
August 31, 1988 - 12:30pm
OCCURANCES (COUNTS/BIN)
1200
1000
800
600
400
200
0
625
645
665
685
705
725
ENERGY LEVEL (DN)
(5 PIXELS/BIN)

FIGURE 3a

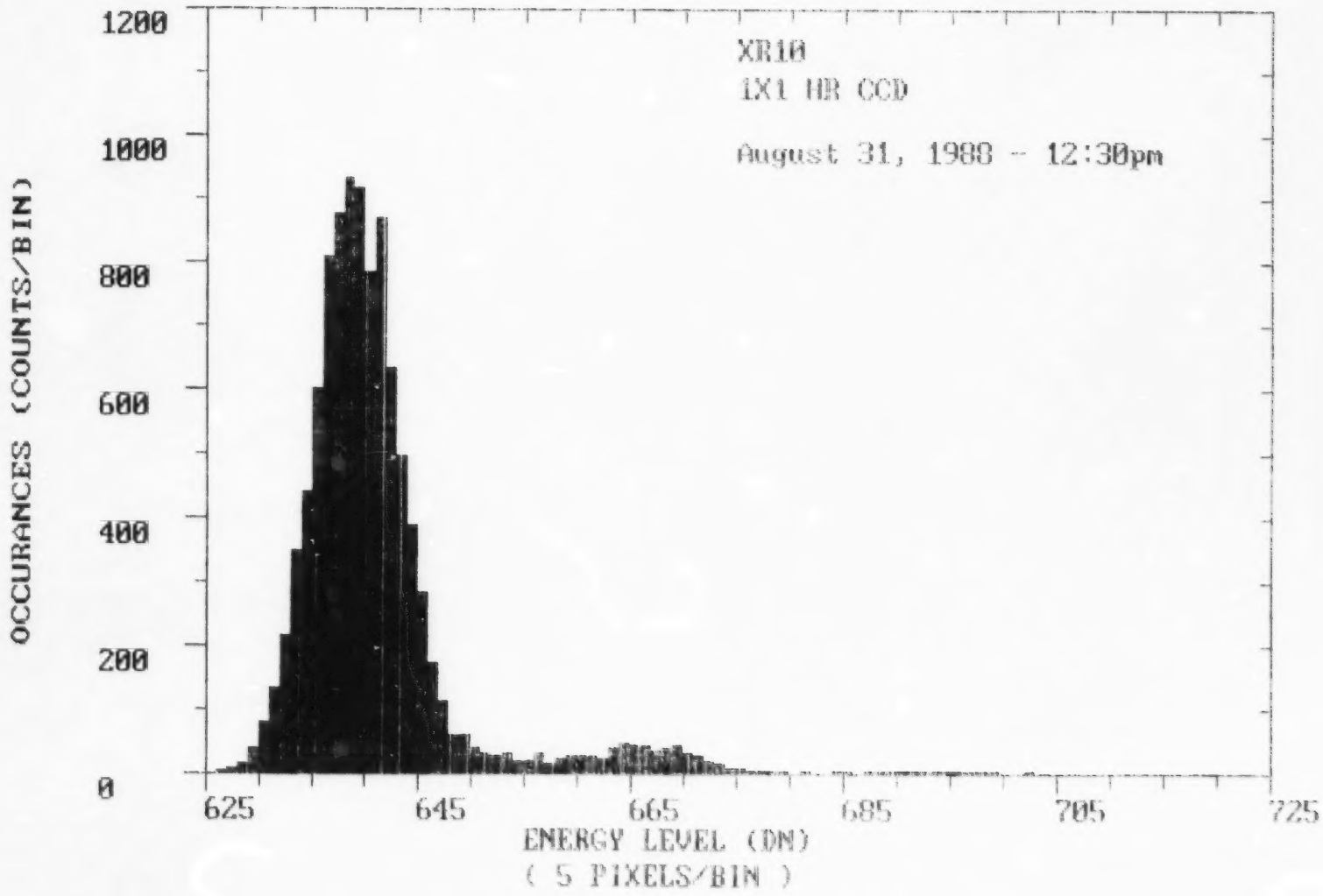
XR10
1X1 HR CCD
August 31, 1988 - 12:30pm
OCCURANCES (COUNTS/BIN)
1200
1000
800
600
400
200
0
625
645
665
685
705
725
ENERGY LEVEL (DN)
(5 PIXELS/BIN)

FIGURE 3b

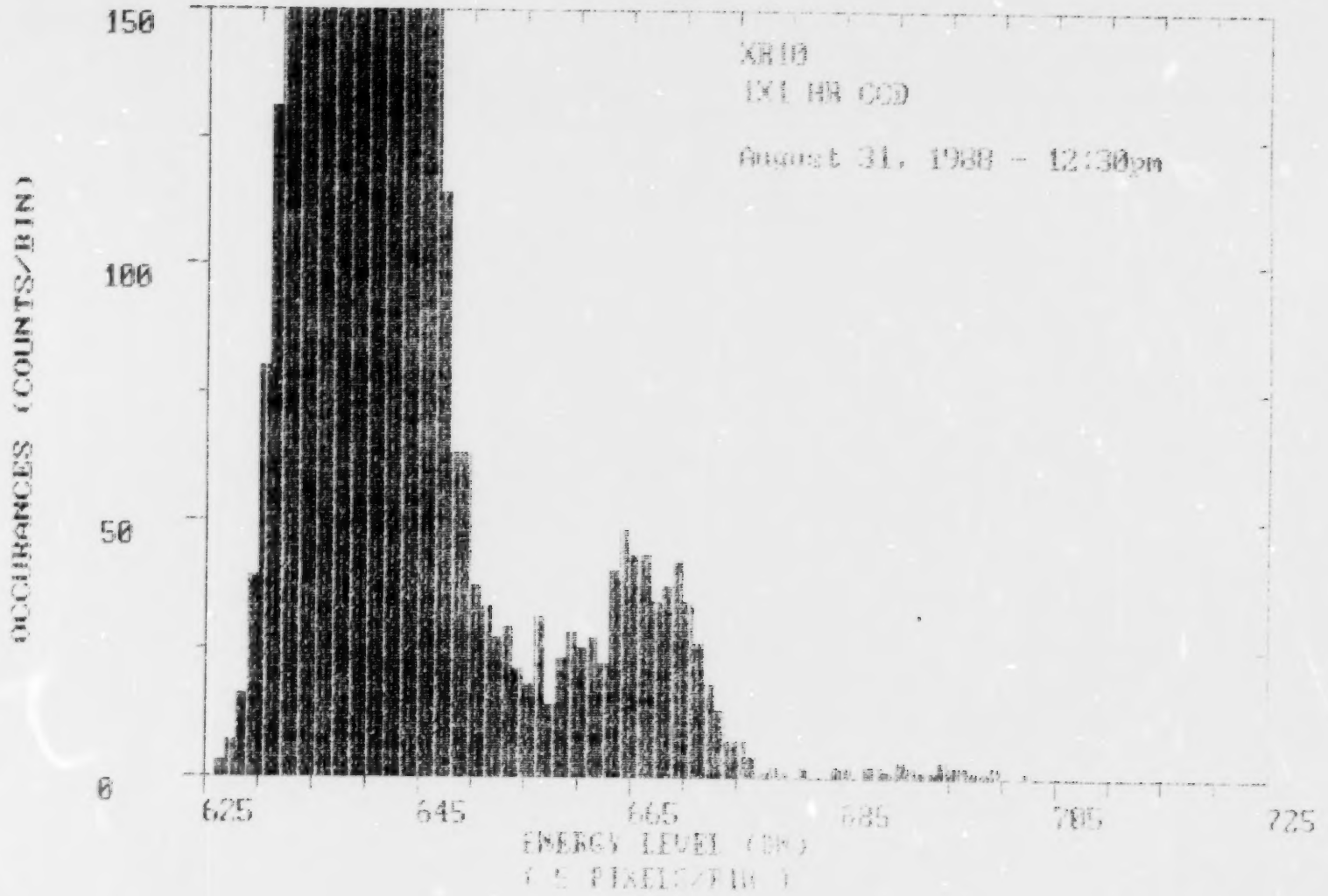
150
100
50
0
OCCURANCES (COUNTS/BIN)
XR1D
IXI HR CCD
August 31, 1988 - 12:30pm
625
645
665
685
705
725
ENERGY LEVEL (eV)

FIGURE 3c

figures #4a, b) The noise in this case essentially appears to swamp the x-ray peak, or more precisely, the dip between the peaks. The noise is higher, and the peak separation is degraded more, than expected. The data are not consistent with the other results. Further investigation is needed to attempt to understand these results.

d) Detection Efficiency Analysis Tests

A quantitative measure of the ability of the CCD to capture x-rays and subsequently collect the charge produced by the event was required. For this purpose, two types of efficiencies are defined. The first, which will be referred to as x-ray detection efficiency, is a measure of the number of non-split events that are observed in the histogram of a particular data set, divided by the number of x-rays estimated to be incident on the front surface of the CCD. This value, n_{xrE} will be compared to n_{xrT}, a calculated value for the number of x-rays absorbed in the depletion region of the CCD, based on the known absorption coefficient of silicon and an assumed depletion depth.

The second type of efficiency to be calculated will be known as the charge collection efficiency. This will be determined by collecting two frames of data, a darkframe and a corresponding x-ray frame, with careful emphasise being placed on keeping all conditions the same. If the location of the dark current peak remains identical in both the x-ray and dark frames , then the increase in the x-ray frame's mean output value is a measure of the effect of x-rays on the data. Converting the increase in dn's to an equivalent number of electrons (multiplying by quantizing step size) and dividing the result by the number of electrons that

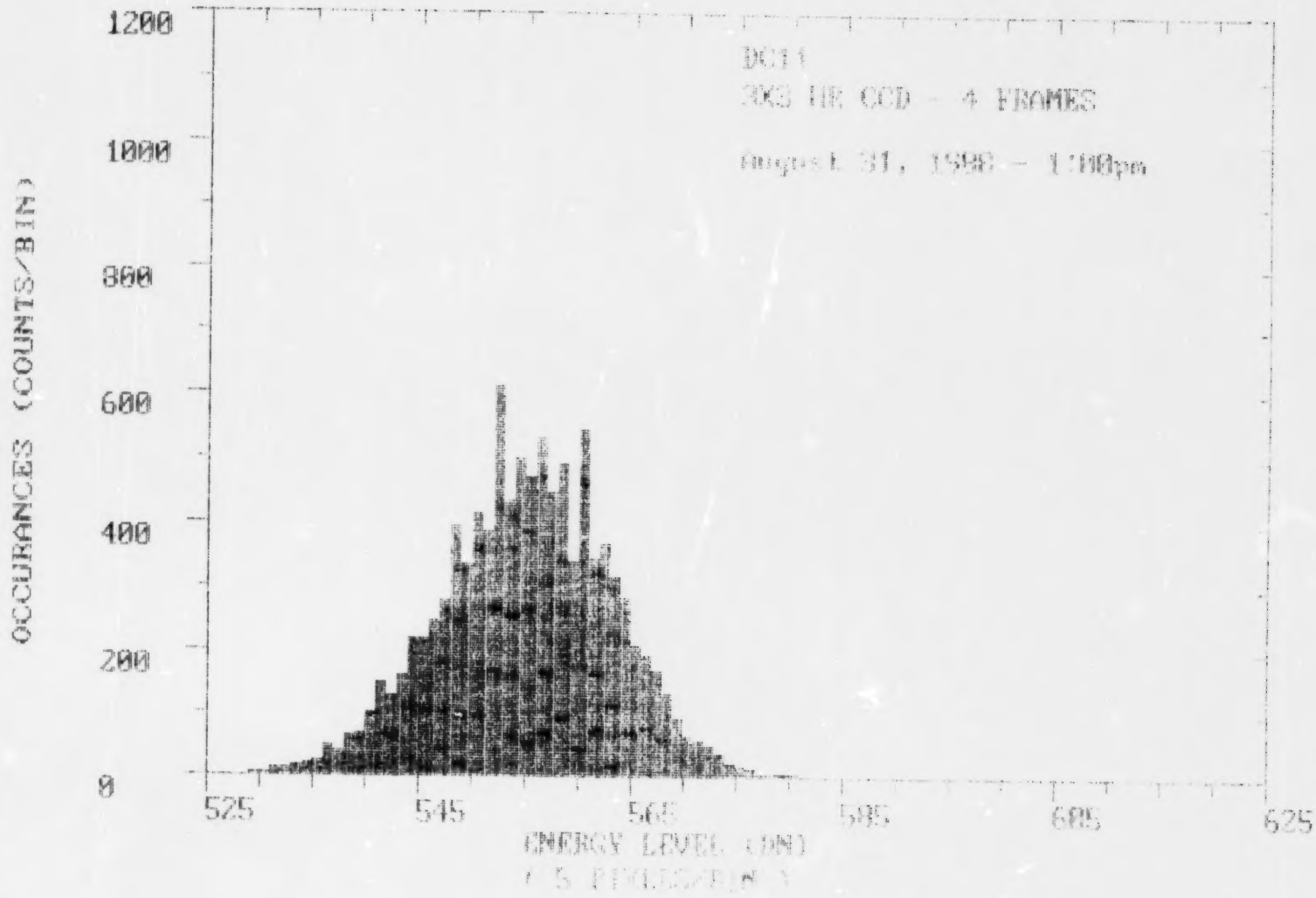
1200
1000
800
600
400
200
0
OCCURANCES (COUNTS/BIN)
525
545
565
585
605
625
ENERGY LEVEL (DN)

FIGURE 4a

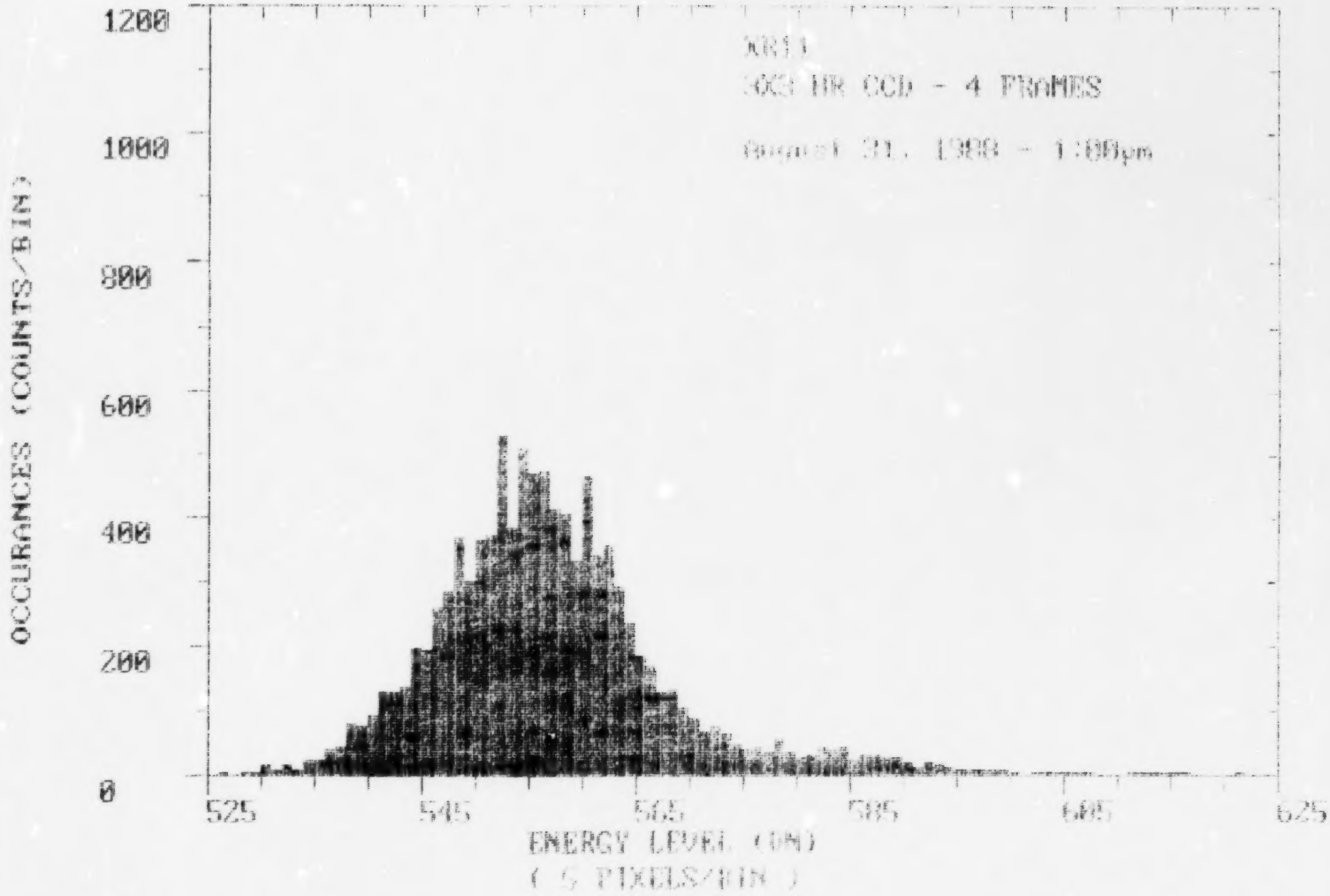
1200
1000
800
600
400
200
0
OCCURANCES (COUNTS/BIN)
525
545
565
585
605
625
ENERGY LEVEL (eV)
(5 PIXELS/BIN)

FIGURE 4b

would be produced if all incident x-rays were absorbed with 100% of the resultant charge collected, gives us the experimental efficiency η_{cE}. This is compared to the theoretical value η_{cT}, derived by estimating the number of x-rays, converted to electrons, absorbed in the active epitaxial layer of the CCD (the depletion and field free regions), divided once again by the amount of charge available in 100% detection.

In short the efficiencies are:

η_{xrT} = Theoretical x-ray detection efficiency

$$= \frac{\text{\# of x-rays estimated to be absorbed in depletion region}}{\text{\# of x-rays incident on CCD}}$$

$$= \frac{\Gamma_T \cdot A_{DR}}{\Gamma_T} = A_{DR}$$

η_{xrE} = Experimental x-ray detection efficiency

$$= \frac{\text{\# of fully collected x-rays detected}}{\text{\# of x-rays incident on CCD}}$$

$$= \frac{N_1 \cdot 1 + N_2 \cdot 2 + N_3 \cdot 3}{\Gamma_T \cdot N}$$

η_{cT} = Theoretical x-ray charge collection efficiency

$$= \frac{\text{estimated charge produced by x-ray absorption in CCD Epi layer}}{\text{charge produced if 100\% of x-rays absorbed in CCD Epi layer}}$$

$$= \frac{\Gamma_E \cdot \varepsilon_{xr}/3.65}{\Gamma_T \cdot \varepsilon_{xr}/3.65} = \frac{\Gamma_T (A_{DR} + A_{FF})}{\Gamma_T} = A_{DR} + A_{FF}$$

η_{cE} = Experimental x-ray charge collection efficiency

$$= \frac{\text{charge collected determined by increase in x-ray frame mean}}{\text{charge produced if 100\% of incident x-rays fully detected}}$$

$$= \frac{\delta x \cdot 1/B}{\Gamma_T \cdot \varepsilon_{xr}/3.65} = \frac{(x_{xr} - x_{df}) \cdot 1/B}{\Gamma_T \cdot \varepsilon_{xr}/3.65}$$

Where the terms utilized in the equation are:

Γ_T = Estimated total x-ray flux rate incident on front surface of CCD.

Γ_E = X-ray flux rate estimated to be absorbed in epitaxial layer of CCD.

A_{DR} = % of Γ_T theoretically absorbed in depletion of CCD region

AFF = % of Γ_T theoretically absorbed in field free region of CCD

N = total number of pixel used in analysis

N_1 = number of pixels to observe a single x-ray event

N_2 = number of pixels to observe a double x-ray event

N_3 = number of pixels to observe a triple or high x-ray event

δx = change in frame mean between a x-ray frame and its corresponding dark frame

x_{xr} = mean of x-ray frame

x_{df} = mean of dark frame

1/B = inverse of system gain
= quantizing step size
= 60 e-/dn

ε_{xR} = x-ray energy
= 5913 ev

As can be seen from the preceding formulas, the structure of the CCD being used needs to be understood. For the purpose of the present experimentation and analysis, the CCD can be looked at as a three layered structure. The top layer,

composed of a complicated structure of electrodes and dielectric layers as described in the Appendix A (Low Energy X-ray Detection), is modelled as a 1.5 μm thick layer of silicon and only serves to block transmission of a portion of the x-rays to the sensitive volume of the CCD. The depletion layer and field free region of the CCD have thicknesses of silicon dependent on specific types of devices. These parameters are given for the two devices tested, as well as the dimension of a yet-to-be fabricated future version of the high resistivity, x-ray-optimized experimental device, in Table #1. With the dimension known, the proportion of the incident x-rays absorbed in each of the layers can be calculated if the absorption coefficient can be determined. The absorption coefficient of an x-ray photon within the range of energies of interest, is given by:

$$\alpha \approx 2.42 \times 10^{[-2.78 \log(\varepsilon) + 4.3]} \qquad \text{for } 1.78 < \varepsilon < 10 \text{ kev}$$

For 5.9 kev x-rays

$$\alpha = .0347\ \mu m^{-1}$$

The amount theoretically absorbed in each layer of each device can be determined, and values are also shown in Table #1.

Utilizing these values in the given efficiency equations, the theoretical efficiencies are determined. These are given in Table #2 along with their corresponding experimental efficiencies calculated using both single pixel data and 3 x 3 super pixel data.

Table #1 - Device Layer Thickness & Absorption For 5.9kev X-rays

Device CCD Layer	Std. CCD		HR_CCD		Future HR_CCD	
	Depth	%Abs	Depth	%Abs	Depth	%Abs
Electrodes & Dielectrics	1.5µm	5%	1.5µm	5%	1.5µm	5%
Depletion	3.0µm	10%	30µm	61%	40µm	71%
Field-Free	22µm	46%	20µm	17%	0µm	0%

% Abs - % Absorption within the layer in question

Table #2 - Device Efficiencies For 5.9kev X-rays

Device Efficiency	Std. CCD		HR_CCD		Future HR_CCD
	1x1	3x3	1x1	3x3	
η_{xrT}	10%	10%	61%	61%	71%
η_{xrE}	16%	40%	30%	25%*	-
η_{cT}**	56%/33%	56%/33%	78%/70%	78%/70%	71%
η_{cE}	48%	50%	53%	38%*	-

*These values are suspect as the data contain an unexpectedly high noise level.

** The first value assumes reflection(no absorption) of the charge at the substrate boundary; the second value assumes absorption at the substrate boundary of 50% of charge produced in the field-free layer. A more complete explanation is given later in this section.

Many things can be determined from the data in these tables. For the standard CCD the observed x-ray detection efficiency (η_{xrE} = 16%) is significantly better than the expected value (η_{xrT} = 10%), suggesting that some of the events occurring in the 'field-free' region are being captured without significant charge spreading or absorption. Results from the 3x3 summation tests are even more dramatic, boosting the efficiency to 40%. For every event occurring in the depletion region, another three events apparently are taking place in the 'field-free' region. These events deliver essential all of their charge into a few near-by pixels. The implication is that there is a transition region extending about half way through the field-free region where there is a residual field sufficiently strong to draw charges upwards into the potential wells for readout, but insufficient to prevent significant spreading of the charges in the process. Alternatively, the charge produced in the field-free region may simply diffuse outwards from the origin, being reflected from the interface between the epitaxial layer and the substrate (see Lumb et al., page 775), and ultimately getting captured (with some losses) in the surrounding pixels. With these possibilities in mind we now turn to the charge collection efficiency results.

In analyzing the values determined for the charge collection efficiency, it is seen that the experimental values are less than the corresponding theoretical values for both devices. η_{cT} is derived assuming that all the charge produced by x-ray absorption in the field-free region is collected. Since the electrons in this situation diffuse radially outward, half of the charge could be expected to diffuse to the back side of the epitaxial layer, away from the depletion layer potential well where the charge is collected for charge transfer.

The charge will be fully collected only if the rear boundary of the field-free region is able to reflect the charge, which is expected to be the case for the p^+ substrate devices employed here (Lumb et al., page 775). (Note in this situation the amount of charge spreading would be considerably more because of the longer diffusion path some of the electrons will have taken prior to being swept into the depletion layer and the potential well.) In some of the other types of CCDs, the backside of the epitaxial layer is considered to absorb the charge that diffuses toward it. In this situation, half the charge produced in the field-free region would be lost. In to Table #2, the two values listed under each column in the n_{CT} row refer to these two extreme situations, the first representing the case for total reflectance of the charge at the rear boundary, and the second referring to total absorption. The equation for the first value is already given. The second value is derived from that to be:

$$n_{CT} = A_{DR} + \tfrac{1}{2} \cdot A_{FF}$$

It is believed that the situation in the devices we used is somewhere between these two extremes. This is consistent with the statement in the previous paragraph where the x-ray detection efficiency was analy. It was suggested that some of the events taking place in the field-free region, probably the ones occurring near to the field-free region - depletion region interface, were being fully collected. The experimentally derived values, n_{CE} = 48%, for the standard device falls between these two extremes, 33% - 56%. Another factor that could effect this value is charge lost due to trapping sites and recombination of the charge carriers. Although this should be of minimal effect in the standard device.

We now consider, in light of the above, the results obtained with the deep-

depletion HR devices. The theoretical x-ray detection efficiency for this device based on the 1 x 1 data is, as hoped, significantly improved (almost doubled) over the standard device's corresponding value. However, the observed 30% value is much less than the expected 61%. There are several possible explanations. The depletion layer thickness of this device is specified to be 30μm. It is possible that this figure, which is not exact, could actually be too large. As well, the large depth of this region may allow for some of the charge to spread into adjacent pixels despite the x-ray being absorbed in the depletion layer. The channel stops running between each column of pixels may be contributing to this. (See Lumb et al., page 777) Finally, as mentioned earlier, the quality of the wafer material in the HR-CCD may not be as high as in the standard CCD, contributing to more of the charge being lost due to trapping sites and recombination of the minority charge carriers. Unfortunately, the effect of using 3 x 3 pixel charge summation cannot be analy because of an unexplained noise problem with the data collected.

The charge collection efficiency results for the HR-CCD suggests that a substantial fraction of the charge produced in the field_free region is lost, even more than would be expected if only half were collected. (η_{CE} = 53% compared to the limits defined for η_{CT} of 70% to 78%.) The amount of charge absorbed in the rear boundary may well be larger in this device, and along with the greater amount of charge lost to trapping sites and recombination, may explain the low experimental value.

IV Conclusions

The foregoing results have significant implications with respect to applications of CCDs to the detection of x-rays. There are several possible scenarios involving combinations of 0-, 1- or 2- dimensional position sensing with either counting of x-rays above a fixed threshold or precise measurement of x-ray energies. These scenarios can be viewed from the perspective of the performance which can be achieved with standard CCD devices, currently available high resistivity devices, or future fully-depleted and/or thinned devices. Performance also depends upon achievable operating temperatures and the quality of the CCD output stages and readout electronics. Readout noise depends in turn on the readout rate, which determines the maximum achievable counting rate, also an important parameter for many applications. Rather than attempting to explore all the branches of this rather complex matrix, we shall confine this discussion to a consideration of some specific implications of our results which bear on the possible uses of CCDs for x-ray detection and measurement.

i. Energy Range

Currently available devices should be effective down to below 1kev. Future thinned devices should operate down to 300ev (75 electrons) and possible lower. System read noise would need to be quite low in order to provide reasonable discrimination at these energies. Thermo-electric cooling would probably suffice, but the low noise levels might require slower readout, limiting count rates to, perhaps, a few thousand per second spread over the array and around one per second in any one pixel.

On the high end the only problem is the rapidly increasing transparency of the CCD. Detection efficiency falls off rapidly above 10kev (110μm absorption length).

ii) Energy Discrimination

Use of on-chip charge summation limits the spatial resolution (66μm for 3x3 summation) but greatly reduces the prevalence of split events, especially those which deliver very small amounts of charge (in the 100 electron range for a 6kev x-ray) to large numbers of pixels. Combining charge summation and deep-depletion devices should minimize charge splitting, making it possible to do a good job of discriminating both energy and positions of individual x-ray events. The present setup (≈ 100 electrons effective noise level) has an effective FWHM of about 1kev. With further work it should be possible to reduce this by up to a factor of 3, while retaining the planned 1 megapixel/sec readout rate capability of the system. It should then be possible to work with (uniform) event rates of up to 10^5/second. The above FWHM estimates should apply reasonably well over the entire energy range, but this has not actually been tested at energies other than 6kev.

iii Photon Counting

If x-rays of fixed energies are present and the only object is to detect their numbers and positions, then noise level requirements are reduced dramatically (for x-rays with energies of a few kev or greater). It is necessary only to define a threshold high enough to avoid responding to noise and split events and low enough to avoid missing events. Depending upon temperature and integration times, pixel or column dependent thresholds may be needed in order

to compensate for dark current. Room temperature operation is conceivable for some applications.

iv) Deep-Depletion (High Resistivity) Devices

EEV have advised us that good quality devices are now available on special order at a premium of several hundred dollars per device. These should have better efficiency and fewer split events, especially when on-chip charge summation is employed.

v) Future CCDs

Larger area devices are currently available and some sample thinned arrays have been produced. Depending upon need it would be possible for ITRES to achieve much improved energy resolution and lower threshold energy, pushing toward the 100ev region, although at considerable slower readout rates and lower temperatures (possibly still in the thermo-electric domain).

APPENDICES

Appendix A

Following are three discussions on key factors affecting the performance of CCD's as detectors of low energy X-rays.

The first describes how device properties such as silicon resistivity and epitaxial layer thickness affect the detection efficiency and energy resolution of the CCD. Backside thinning is also discussed.

In the second section, the role of dark current in determining the overall system noise level is discussed. The amount of cooling required in order to discriminate, reliably, true X-ray events from dark current fluctuations is also considered. One interesting conclusion is that room temperature operation may be feasible in some circumstances.

The third section discusses the principal factors which limit the response of the CCD to low energy X-rays.

Prospects for X ray CCD's

The future prospects for X ray CCD's with good efficiency and energy resolution, are driven mainly by current efforts to develop CCD's utilizing very high resistivity silicon. Proper detection of X ray events requires that the X rays be absorbed within the depletion layer of the CCD.

High resistivity silicon epitaxial material is useful for X ray observations mainly because it provides a deeper depletion depth for the same applied voltage conditions, when compared to a standard resistivity device, resulting in the absorption of more X rays and giving a higher detection efficiency. The depletion depth in silicon is defined as :-

$$D_d = [\ 2\ k_{si}\ \varepsilon_o\ (\ V_o - V\ )\ /\ q\ N_b\ ]$$

where
- k_{si} is the relative permittivity of silicon
- ε_o is the permittivity of free space
- V_o is the contact potential
- V is the applied potential
- q is the electronic charge
- N_b is the ion concentration from doping sources in the bulk.

Relating the ion concentration in the bulk, to the material resistivity through the approximate relationship :-

$$N_b = 2.5 \times 10^{16}\ R^{-1.2}$$

where
- N_b is the ion concentration (cm^{-3})
- R is the material resistivity (Ωcm)

which gives the relationship :-

$$D_d = C\ (\ V_o - V\ )^{0.5}\ R^{0.6}$$

where
- C is a constant of value 0.23 when R is measured in Ωcm and V_o and V are measured in volts
- D_d is the depletion depth in μm.

Using values typical for CCD's of $V_o \approx 16.5$ V and $V \approx 12$ V this gives :-

D_d (μm)	R (Ωcm)
2.0	10
3.0	20
3.5	30
8.0	100
31.0	1000
39.7	1500
82.0	5000

For normal visible imaging with CCD's the advantage of having a deep depletion depth is twofold. Firstly, looking at the absorption coefficients for incident radiation, most visible light is absorbed near the surface. The near infra red, however, is absorbed much deeper in the silicon as the material becomes transparent to the infra red region of the spectrum. This results in de-focusing or resolution loss due to charge diffusion from the field free region into the shallow depletion region, a mechanism similar to event charge splitting in X ray detection. The following table shows the variation of absorption depth with wavelength for visible and near IR radiation.

$1 / \alpha$ (µm)	Wavelength (nm)
0.1	400
4.3	600
23.0	800
572.0	1000

The absorption of blue light in the electrode structure overlying the active region of the CCD leads us to the second advantage of high resistivity materials. In order to improve blue sensitivity, CCD manufacturers are attempting to thin their devices. Thinning, permits illumination from the back surface of the device, thus eliminating the absorption of blue light in the overlying Poly-silicon electrode structure. The required thickness, necessary for good sensitivity and resolution, depends on the depletion depth. The dependence arises because electron-hole pairs generated near the back surface by blue radiation, have to diffuse toward the front of the CCD to be captured in a depleted well. The distance the electron is required to diffuse over is given by the difference between the material thickness and the depletion depth, minus a small amount accounted for by back surface effects and treatments. For the best performance this electron diffusion path must be kept small, to eliminate recombination and resolution loss effects, or ideally eliminated completely by fully depleting the material.

A larger depletion depth, thus allows a thicker thinned device and hence greater physical strength of the thinned device along with a simpler, higher yield thinning process. At EEV, Chelmsford, UK, 5000 Ωcm material has been processed and thinned to approximately 100 µm. The resultant devices are nominally 80% depleted. Problems arise, however, when 100% depletion is attempted due to crystallographic defects at the back surface along with the not-too-well understood physics of the back surface, injecting dark current into the depletion region.

The largest problem with high resistivity silicon is material quality and availability. High resistivity silicon is very difficult to manufacture as the impurity concentrations are very low indeed, for 1000 Ωcm material only one in every 8×10^9 atoms are dopant material compared to one in every 3×10^7 for 10 Ωcm material. The quality of these material wafers is generally low because, being produced in small lots , they do not benefit from a steady, well calibrated process. Residual contaminants in the processing facility make the control over the material resistivity very difficult indeed.

Work currently in progress at EEV, Chelmsford, UK and their silicon

suppliers, is to provide CCD's made with silicon of 1500 Ωcm, 40 μm epitaxial thickness to be easily available on a special order basis. It is expected that standard production will move from 20 Ωcm, 25 μm epi. material to 100 Ωcm, 25 μm epi. The limit of 100 Ωcm material arises because this is the highest resistivity material freely available from the silicon suppliers. This technology advancement toward high resistivity material is clearly directly relevant to providing superior X ray devices. Currently only a few high resistivity devices, made at EEV, are available for testing as so far the majority of the development of these devices has been carried out for ESTEC in europe in conjunction with Leicester University. This situation is expected to change in the near future as EEV have currently procured their own high resistivity Silicon and are in progress with production on this Silicon.

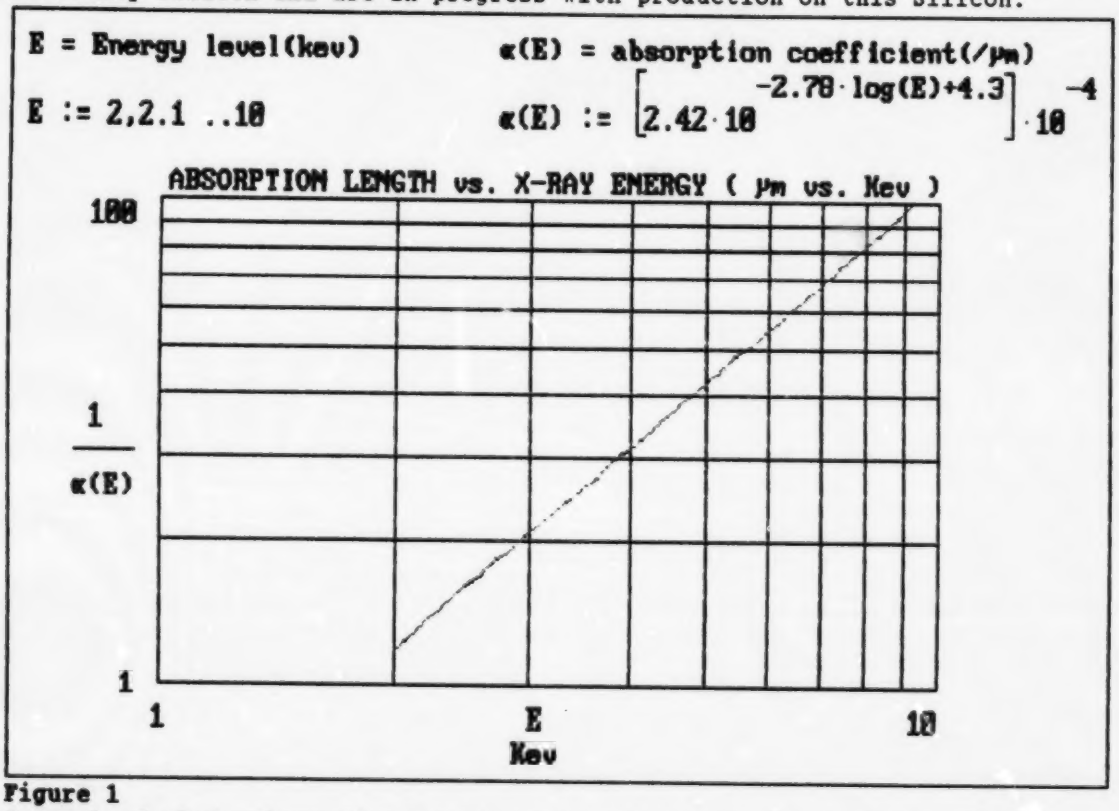

Figure 1
A graph of photo-absorption length against incident X ray photon energy

Dark Current

The limit to the ability to measure X ray energies using Silicon detectors lies in the readout noise of the system. The noise floor of most CCD systems is dominated by the output transistor of the CCD. Other contributions from the analog signal chain and the supporting electronics can be kept to a minimum by careful design techniques. The noise floor achieved by the ITRES camera system is measured, using a signal/variance technique, at approximately 100 electrons (70 electrons for the standard device and 160 electrons for the high resistivity device).

In most realistic situations, device dark current contributes to the noise level. The noise on the dark current is mainly shot noise, which is Poissonian in nature. Other noise sources do exist, such as material defects and other pixel non-uniformities, however, these are device dependent and can only be discussed qualitatively. Experience dictates that dark current shot noise dominates on systems that are uncooled and have no obvious dark current defects.

The magnitude of dark current present on EEV devices is described by the well known exponential equation :-

$$I_d = A \exp(- V_{bg} \, q / 2 \, k \, T)$$

where A is a constant having the value 1.5×10^{14} if I_d is measured in electrons per pixel per second
V_{bg} is the effective channel to gate voltage
q is the electronic charge
k is Boltzman's constant
and T is the temperature.

Taking some typical values :-

$V_{bg} = 1.1$ V
$q = 1.6 \times 10^{-19}$ C
$k = 1.3 \times 10^{-23}$ J/K

gives :-

$$I_d = 1.5 \times 10^{14} \exp(-6.8 \times 10^{3} / T)$$

and hence the noise level expressed in electrons (square root) of :-

$$N_{dc} = (I_d)^{0.5} = 1.2 \times 10^{7} \exp(-3.4 \times 10^{3} / T).$$

The following graphs show the system noise as a function of temperatures.

$$\text{Noise}_{\text{Temp}} := \left[\text{SystemNoise}^{2} + 1.5 \cdot 10^{14} \cdot \left[\frac{\exp\left[-6.8 \cdot \frac{10^{3}}{\text{Temp}} \right]}{\frac{1}{\text{IntegrationTime}}} \right]^{0.5} \right]$$

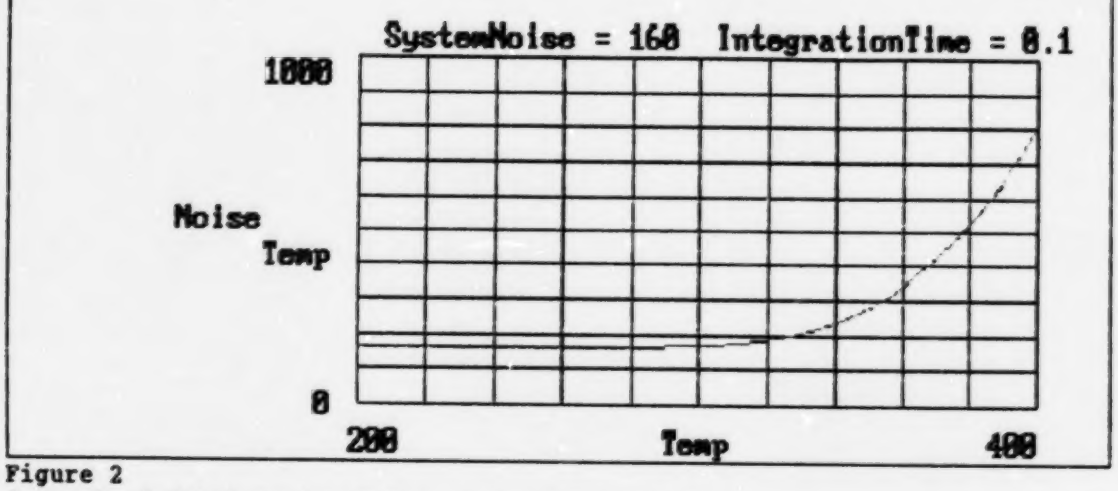

Figure 2
A graph of Total System Noise versus Temperature

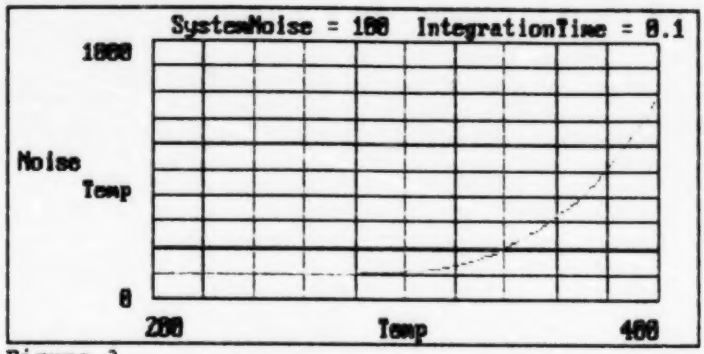

Figure 3
A graph of Total System Noise vs. Temperature

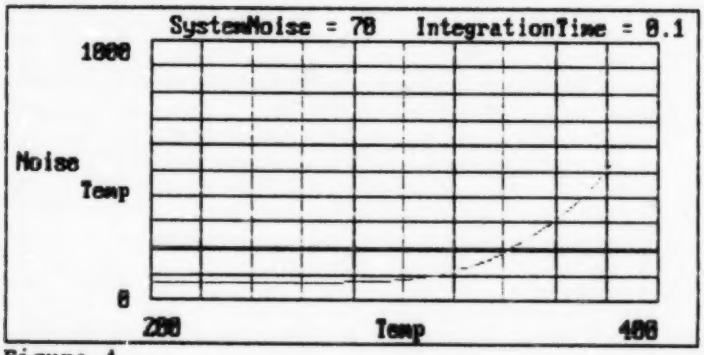

Figure 4
A graph of Total System Noise vs. Temperature

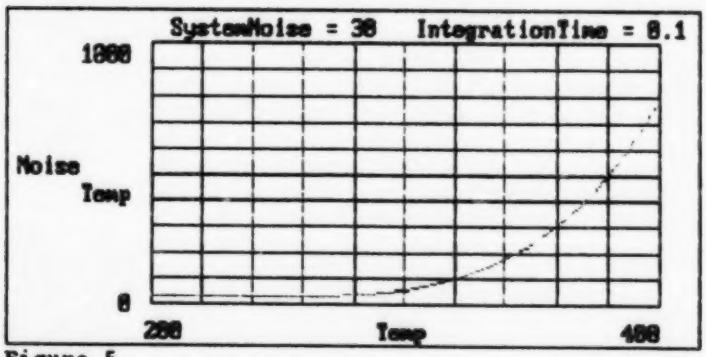

Figure 5
A graph of Total System Noise vs. Temperature

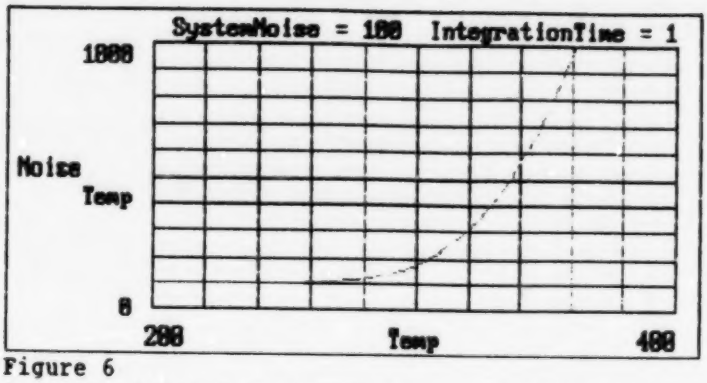

Figure 6
A graph of Total System Noise vs. Temperature

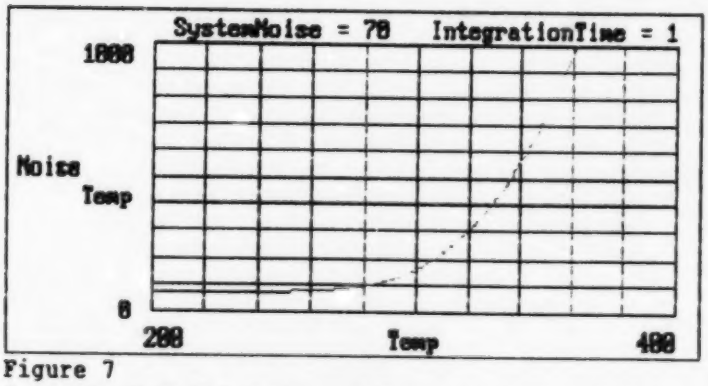

Figure 7
A graph of Total System Noise vs. Temperature

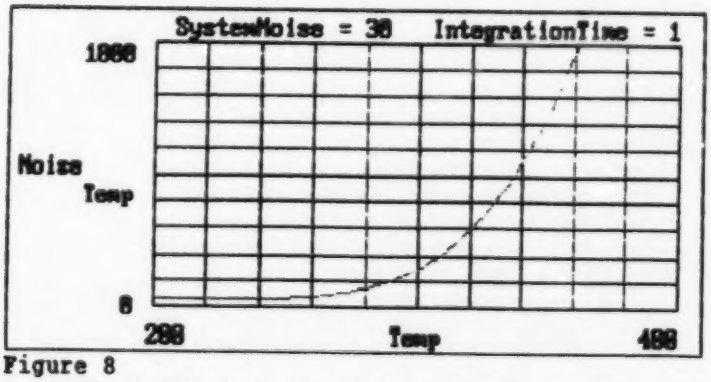

Figure 8
A graph of Total System Noise vs. Temperature

It is clear that above approximately 300 K the dark current shot noise dominates, and below this level, the system readout noise dominates. For operation above 300 K the effective contribution from dark current shot noise can be reduced, by reducing the integration time.

X ray photons are absorbed by imparting their energy to inner shells of electrons in silicon atoms of the lattice. These energetic electrons, in turn, excite a chain of outer valence electrons in nearby atoms into the conduction band, through a series of quasi-elastic Rutherford scattering collisions. This mechanism efficiently distributes the X ray energy into a number of excitations, allowing the X ray energy to be measured. By assuming the energy is distributed to the smallest detectable event, the release of a valence electron to the conduction band at 3.65 eV per event, the total X ray energy is given by the total number of excited electrons multiplied by 3.65 eV. This tells us that a 5.9 KeV X ray photon will produce 1600 electrons per event.

The noise of this process is not described by pure Poissonian statistics but follows a modified Poissonian reduced in width by the Fano factor. The FWHM size of an X ray peak is then described by the equation :-

$$\delta E = 2.35\ W\ (\ n^2 + N_{dc}^2 + f\ (\ E\ /\ W\ )\ )^{0.5}$$

where
- W is the conversion factor (3.65 eV / electron)
- n is the system noise (electrons)
- N_{dc} is the dark current noise (electrons)
- f is the Fano factor (= 0.12)
- E is the X ray peak energy (eV),

hence, for a system with 70 electrons noise and negligible dark current noise, the expected peak FWHM is 612 eV (168 electrons), for a noiseless system the value would be 119 eV (33 electrons).

Assuming, the system noise is given by the quadrature sum of the read-noise and the dark current noise the FWHM of the dark current peak is given by :-

$$N_{total} = (\ n^2 + N_{dc}^2\ )^{0.5}$$

In order to be able to detect an X ray peak, the separation between the dark current peak and the X ray peak must be greater than the sum of the two peak's full width half maxima, hence the separation must be :-

$$S \geq 2.35 \times 3.65 \times (\ n^2 + N_{dc}^2\ )^{0.5} + \delta E$$

$$S \geq 8.58 \times (\ n^2 + (\ 1.5 \times 10^{14} \times IT \times \exp(\ -6.8 \times 10^3\ /\ T\ )\ )\ )^{0.5}$$

$$+$$

$$8.58 \times (\ n^2 + (\ 1.5 \times 10^{14} \times IT \times \exp(\ -6.8 \times 10^3\ /\ T\ )\ ) + 0.12 \times (\ E\ /\ 3.65\ ))^{0.5}$$

Solving this equation for T using :-
n = 70 electrons
E = 5900 eV
IT= 0.1 secs
S = 1600 electrons,

we get (figure 9) a temperature of 363 K.

$T := 363$ Temperature $E := 5900$ X ray energy $It := 0.1$ Integration Time

$SN := 70$ System Noise $W := 3.65$ Conversion factor

$$XFWHM := 0.58 \left[SN^2 + \left[1.5 \cdot 10^{14} \cdot It \cdot \exp\left[-6.8 \cdot \frac{10^3}{T} \right] \right] + 0.12 \cdot \left[\frac{E}{W} \right] \right]^{0.5}$$ X ray peak FWHM

$$DFWHM := 0.58 \left[SN^2 + \left[1.5 \cdot 10^{14} \cdot It \cdot \exp\left[-6.8 \cdot \frac{10^3}{T} \right] \right] \right]^{0.5}$$ Dark Current FWHM

$SEPERATION := XFWHM + DFWHM$ Minimum detection criteria in eV

$$Sep_elec := \frac{SEPERATION}{3.65}$$ in electrons

$SEPERATION = 5.814 \cdot 10^3$ eV $Sep_elec = 1.593 \cdot 10^3$ electrons

Figure 9
Solution and equation, showing maximum temperature operation for 5.9 KeV X ray detection

Low Energy X ray Detection

The limit to detection of low energy X rays with CCD's, is because of absorption in the overlying electrode structure, a problem identical in nature to blue response of CCD's. In order to explain this further let us look at the details of the overlying structure.

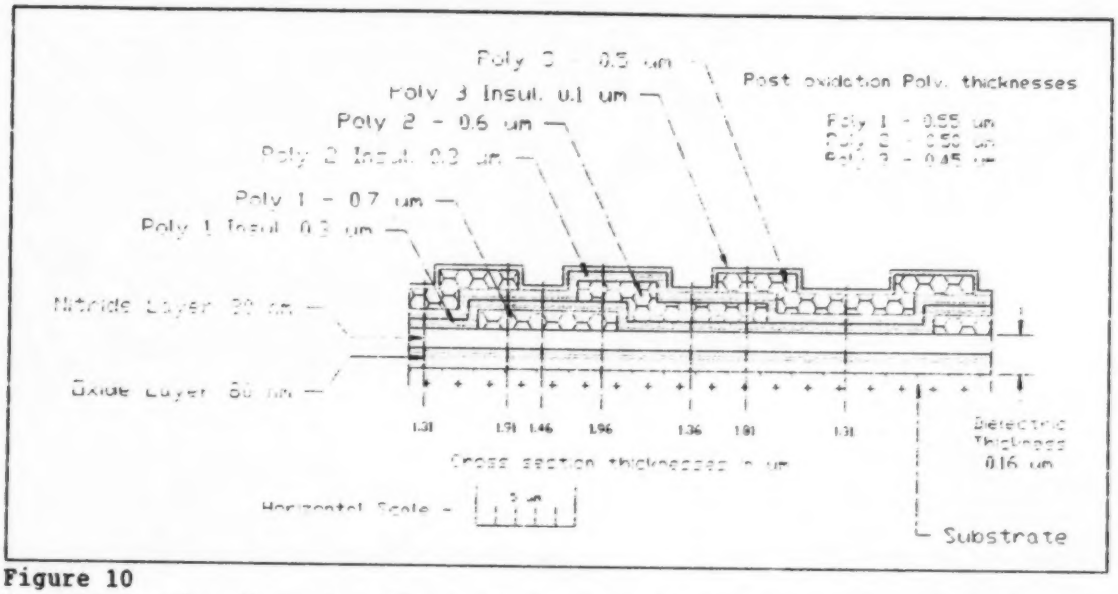

Figure 10
A cross section through a 22 um pixel, showing the electrode and dielectric thicknesses.

The Polysilicon electrodes and the Silicon Dioxide dielectric have the same absorption coefficients as Silicon. The low energy absorption coefficients for Silicon are tabulated below :-

X ray energy (eV)	Absorption Coefficient (um^{-1})
3000	0.228
2500	0.378
2000	0.703
1800	0.942
1500	0.126
1200	0.228
1000	0.372
800	0.681
500	2.336
300	75.314
100	303.659

The feature in the absorption coefficient at 1838 eV is due to an absorption edge corresponding to the K edge in the Silicon electron structure.

The L edge falls at 118 eV, reducing the coefficient temporarily for falling X ray energies.

As the overlying electrode structure is approximately 2 um thick, photons of energies such that their absorption coefficient is greater than 0.5, will not penetrate effectively. This radiation will be absorbed in the electrode structure and lost. Thus for exposure through the front surface of the CCD structure the useful band is defined as approximately 800 eV to 10000 eV, with a sharp drop in quantum efficiency at the Silicon K edge at 1838 eV. CCD's also are sensitive to radiation just below the L edge at 118 eV for a range of approximately 60 eV to 118 eV.

As previously mentioned, absorption of blue light in the overlying electrode structure drives CCD manufacturers to thin their devices and illuminate onto the rear surface of the CCD such that the only losses are in the native oxide of the Silicon substrate and any 'dead layers' at the back surface. The same approach is useful for the detection of low energy X rays. It is hoped that the thinning of high resistivity devices, to obtain a fully depleted detector, will produce X ray sensitivity in the range of 300 eV to 10000 eV with a reasonable QE throughout that range. The 300 eV lower limit represents a sizeable technical challenge as the effective dead area, including the native oxide, must be less than 13 nm ! for reasonable efficiency.

Appendix B

Related Scientific Papers

1) Lumb et al. "X-ray Measurements Of Charge Diffusion Effects In EEV Ltd. Charge-Coupled Devices"

2) Janesick et al. "Charge-Coupled Device Advances X-ray Scientific Applications In 1986"

X-ray measurements of charge diffusion effects in EEV Ltd. charge-coupled devices

David H. Lumb, MEMBER SPIE
Eric G. Chowanietz
Alan Wells
Leicester University
Physics Department
X-ray Astronomy Group
Leicester LE1 7RH, England

Abstract. Most scientific imaging applications of CCDs require low noise and high charge transfer efficiency. These attributes have been exhibited in devices produced by a number of manufacturers, but not all perform well as x-ray imaging spectrometers. This application requires that all charge liberated by an x-ray photon be completely collected within the original pixel. Processes of charge diffusion may prevent this from occurring and degrade the obtainable energy resolution. Measurements of charge diffusion and its effect on x-ray performance are presented for three types of English Electric Valve Co. (EEV) CCDs. These are fabricated on bulk and epitaxial wafers with resistivities of 1000 and 10 Ω cm. A range of different pixel sizes is employed. Measurements of detection efficiency are compared with predictions of a theoretical charge-diffusion model. Implications for optimizing the CCD structure for use in an x-ray astronomical spectroscopy application are noted.

Subject terms: charge-coupled devices; x-ray imaging; x-ray spectroscopy; astronomy; charge diffusion.

Optical Engineering 26(8), 773-778 (August 1987).

CONTENTS

1. Introduction
2. Theory
   2.1. Charge diffusion in the depletion region
   2.2. Charge diffusion in the field-free region
3. Experiment
4. Results
5. Discussion and summary
6. Acknowledgments
7. References

1. INTRODUCTION

Previous spaceborne observations dedicated to the study of x-ray astronomy have generally fallen into one of two categories: survey missions designed to discover and catalog sources and observatory-type missions dedicated to detailed studies of small numbers of objects. In both categories, subject to the availability of suitable technology, imaging instruments have been employed to study the spatial detail of the observed source and also to take advantage of the much superior sensitivity and background rejection properties of imaging systems. The most advanced observatory conceived to date is NASA's Advanced X-ray Astrophysics Facility (AXAF), in which the proposed AXAF CCD Imaging Spectrometer (ACIS)[1] instrument is based on a CCD detector.

Invited Paper CC-110 received Dec. 8, 1986; revised manuscript received March 4, 1987; accepted for publication March 30, 1987; received by Managing Editor April 6, 1987.
© 1987 Society of Photo-Optical Instrumentation Engineers.

Complementary to AXAF is the European Space Agency (ESA) cornerstone mission X-ray Multi-Mirror (XMM),[2] dedicated to x-ray spectroscopy. With this mission the physics of astronomical objects may be revealed by plasma diagnostics made possible by detailed examinations of the x-ray spectra. This objective requires high-throughput optics whose design sacrifices spatial resolution in return for a greatly increased effective collecting area. A number of identical mirror modules will provide 30 arcsec imaging (~1 mm in the focal plane) and an 8000 cm^2 collecting area. The main emphasis of the mission is to perform broadband spectroscopy in the 0.2 to 10 keV band (50 to 1 Å), with moderate energy resolutions in the range $E/\Delta E = 5$ to 60. It is for this mission that the developments described herein are being undertaken.

Imaging gas counters have been employed for many years in x-ray astronomy but are not able to provide the required resolving power. Energy dispersive Si(Li) diode spectrometers,[3] on the other hand, have no inherent imaging ability. Hence, CCDs are being examined for this application.

Silicon absorbs an x-ray photon with the release of an electron hole pair per 3.65 eV of photon energy. The theoretical limit to energy resolution is determined by the statistics of pair creation, with the full-width at half-maximum (FWHM) resolution defined by

$$\Delta E = 2.35 \times 3.65 \sqrt{N^2 + \frac{FE}{3.65}} \,. \qquad (1)$$

where E is the photon energy, F the Fano factor (~0.1), and N the readout noise. When operated in a photon counting mode, CCDs can provide not only the inherent imaging response but also a measurement of the photon energy.

In all CCDs the noise characteristic of the readout degrades the energy resolution, but in the best devices the noise is less than 10 electrons rms, and a resolution of 130 eV should be readily attainable at the astrophysically important iron emission line at 6.7 keV. The resultant resolving power $E/\Delta E \sim 50$ is sufficient to separate the most important components of the iron line complex.

In practice, other effects may combine to degrade the attainable resolution by preventing a correct measurement of the charge deposited by a photon. For example, imperfect charge transfer efficiency (CTE) causes charge to be lost, which leads to an underestimate of photon energy. Also, the noise figure is degraded by spatial variations in CTE or by shot noise on the number of charges lost. Furthermore, photogenerated charge may radially diffuse or partially recombine before collection at the buried channel. The loss of charge or splitting between pixels also leads to underestimation of energy and a degradation of resolution because the amount of charge lost varies with the location of the charge generation event.

The means of obtaining low read noise and high CTE in CCDs has been extensively studied, and the devices have been significantly improved for optical applications. Charge collection efficiency is less well understood, and this work attempts to provide some modeling for, and measurements of, the effect.

2. THEORY

2.1. Charge diffusion in the depletion region

Previous work has aimed at modeling the process of charge diffusion within the depletion region,[4] by employing a Monte Carlo simulation. Here, an analytical treatment is presented, considering a plane parallel depletion layer of depth x_d. Figure 1 shows a cross section of a typical CCD. A simple linear field distribution is assumed such that the drift velocity of a charge packet is given by

$$V_{drift} = -\frac{\mu e N_A}{\epsilon} x \, . \tag{2}$$

Solving for the time to drift a distance x, we have

$$t = -\frac{\epsilon}{\mu e N_A} \ell n\left(\frac{x_d - x}{x_d}\right) . \tag{3}$$

where ϵ, μ, e, and N_A are the permittivity, mobility, electronic charge, and acceptor concentration of the silicon. The radial distribution of charge after this drift time is given by

$$q(r') \propto \exp\left(\frac{-r'^2}{4Dt}\right) . \tag{4}$$

where D is the electron diffusion constant.

It should be noted that the radial distribution of charge given by Eq. (4) is collected in the plane of the buried channel. To derive the projected charge distribution (see Fig. 2), we must evaluate the integral

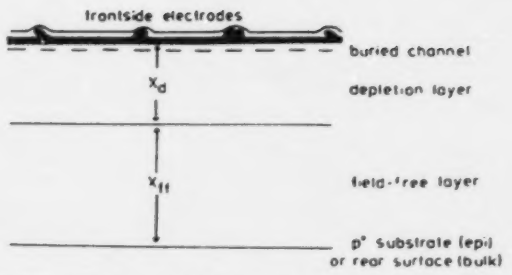

Fig. 1. Cross section of a typical CCD, showing the significance of variables used in the analysis in Secs. 2.1 and 2.2.

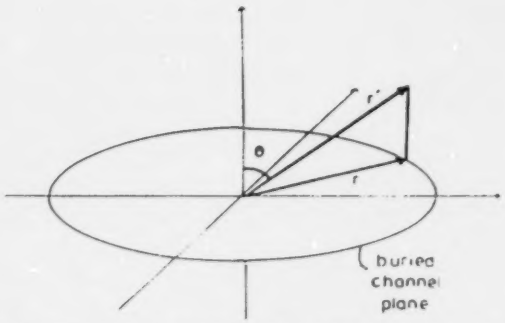

Fig. 2. Projection of the spherical charge distribution onto the buried channel plane.

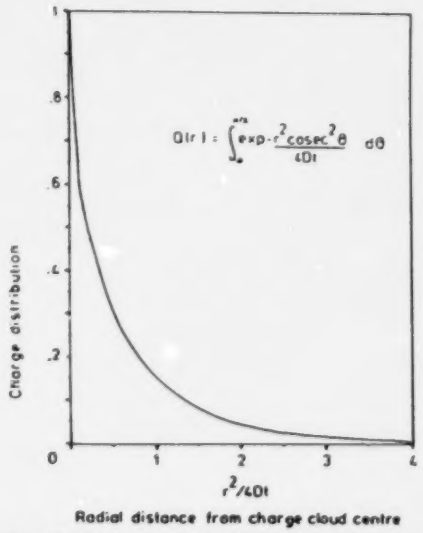

Fig. 3. Radial distribution of charge in the buried channel plane following drift across the depletion layer.

$$Q(r) = \int_0^{\pi/2} \exp\left(\frac{-r^2 \csc^2\theta}{4Dt}\right) d\theta \, . \tag{5}$$

The numerical evaluation of this expression is described in Fig. 3. Note that this is not a Gaussian distribution; however, to

compare with the "2-sigma diameter" of the Janesick et al. model,[4] we take the point $Q(r) = 0.6$ and find $r^2/4Dt \sim 0.1$, i.e.,

$$r = \sqrt{\frac{-0.4 D\epsilon}{\mu e N_A} \ln\left(\frac{x_d - x}{x_d}\right)} . \quad (6)$$

or we substitute $D/\mu = kT/e$, which yields

$$r = \sqrt{\frac{-0.4 \epsilon kT}{e^2 N_A} \ln\left(\frac{x_d - x}{x_d}\right)} . \quad (7)$$

For $x/x_d = 0.5$ and $N_A = 10^{15}$ cm^{-3}, we obtain a 2-sigma diameter of 1200 Å, compared with the Janesick et al.[4] estimate of 600 Å.

2.2. Charge diffusion in the field-free region

Janesick et al.[4] also modeled the diffusion of charge in a field-free layer, taking the case of a back-illumination CCD with a reflecting rear boundary. This model is also a good approximation for the case of a p-type field-free epitaxial layer overlying a p^+ substrate. The expression obtained for the 2-sigma diameter of the charge cloud diffusing from a depth x in a field-free layer of depth x_{ff} was

$$C_{ff} = 2x_{ff}\sqrt{1 - \left(\frac{x}{x_{ff}}\right)^2} . \quad (8)$$

For bulk silicon devices, or p-type epitaxial material on n^+-type substrates, the rear boundary may be absorbing.[5] For this case, we have shown by similar modeling that the corresponding expression is

$$C_{ff} = x_{ff}\sqrt{1 - \left(\frac{x}{x_{ff}}\right)^2} . \quad (9)$$

These models neglect charge recombination, and a more precise description of the charge diffusion is given in analytical treatments presented by Hopkinson.[5,6] The fractional pulse heights of charge packets intercepted at the depletion boundary are defined as the fraction of the photoelectrons that are eventually detected at the depletion layer boundary and are denoted h(x).

Again, the radial spread is not strictly Gaussian; however, we use the approach of Janesick et al.[4] to project a series of Gaussian distributions onto a grid of pixels. The pulse height distributions expected from a set of monochromatic x-ray inputs at a random set of photon absorption coordinates can then be modeled by calculating the fraction of the Gaussian intercepted by a pixel and then scaled by the appropriate expression for fractional pulse height due to recombination effects.[5]

Figure 4 plots the radial spread of charge as a function of absorption depth for two of the devices used in this work. The P8603 and P8600HR devices have depletion depths of 3 and 30 μm, respectively (resistivities of 10 and 1000 Ω cm). The data show that in each case the greatest contribution to radial spread comes from the field-free layers. For comparison, the photon energy is noted, for which the absorption depth corresponds with the 1 e absorption length in silicon.

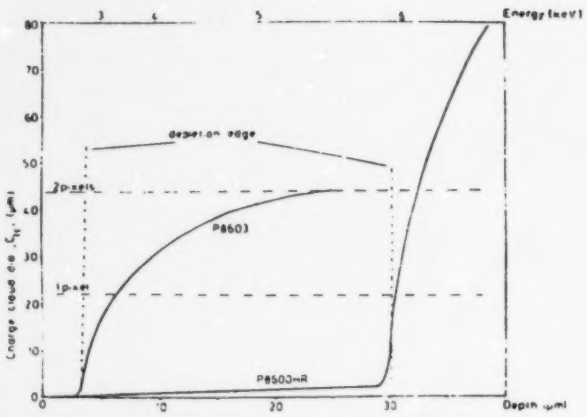

Fig. 4. Variation of radial spread with absorption depth. Details of the device structures are contained in the text. Energy equivalent scale denotes the 1/e attenuation length in silicon.

3. EXPERIMENT

Over the past five years the Leicester University X-ray Astronomy Group has been investigating the x-ray response of CCDs fabricated by General Electric Co. (UK). These devices are now produced by English Electric Valve Co. Ltd. and marketed as the P8600 series imagers. Data reported here were obtained from three types of P8600 devices.

The P8603 is the European TV format device, which in full-frame mode has 578 × 385 pixels, each 22 μm square. The device is front illuminated through a three-phase polysilicon electrode technology. The depletion layer is nominally 3 to 5 μm thick ($N_A = 10^{15}$ cm^{-3}, or 10 Ω cm) and is contained within a p-type epitaxial layer that is approximately 25 μm thick, which itself overlies a low-resistivity p^+ substrate. The devices employed were preselected for good low-light-level performance.

The P8607 is fabricated with identical technology and represents a 3/4 linearly scaled version of the P8603. The resulting pixel size is 16.5 μm square.

The P8600HR is an experimental device fabricated for the Leicester group. It is identical to the P8603 except for the starting wafers. These are 1000 Ω cm ($N_A \simeq 10^{13}$ cm^{-3}) bulk silicon, with an expected depletion depth of ~30 μm. Identical processing was applied to wafers of both resistivities. Before packaging, the wafers were lapped to a thickness of ~300 μm.

To minimize dark current, the devices were cooled in operation by mounting the packages inside a vacuum cryostat with a temperature-controlled cold element. A temperature of 170 to 180 K was maintained, at which the on-chip MOSFET noise (7 to 9 electrons rms) was generally found to be minimized in EEV devices.

The sequences for control of readout were held in fast RAMs and downloaded from the experiment microcomputer. This enabled features such as the binning of pixels to be employed. By combining the signals from neighboring pixels, on chip, different effective pixel sizes were obtained.

Low-noise drive electronics and a dual-slope integrator were employed, with a system noise of approximately 3 elec-

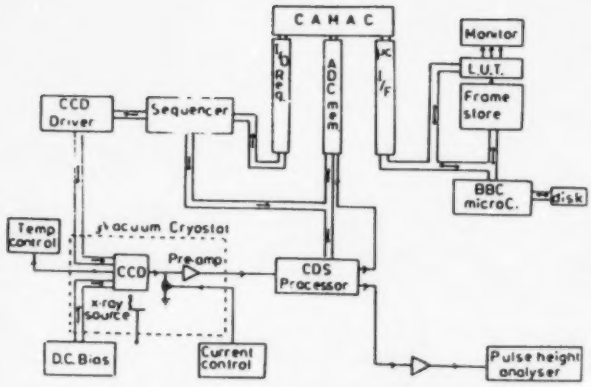

Fig. 5. Schematic of the experimental arrangement.

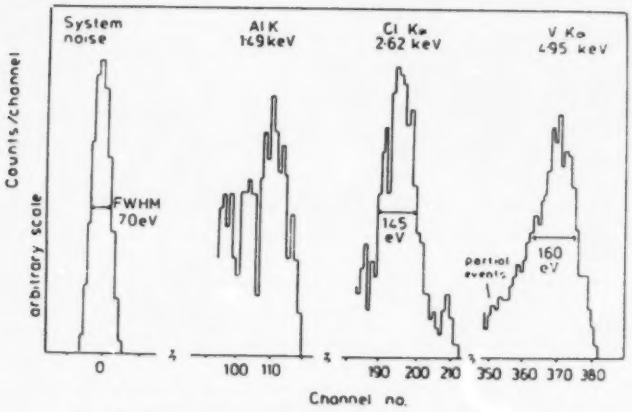

Fig. 6. Raw pulse height distributions for the P8607.

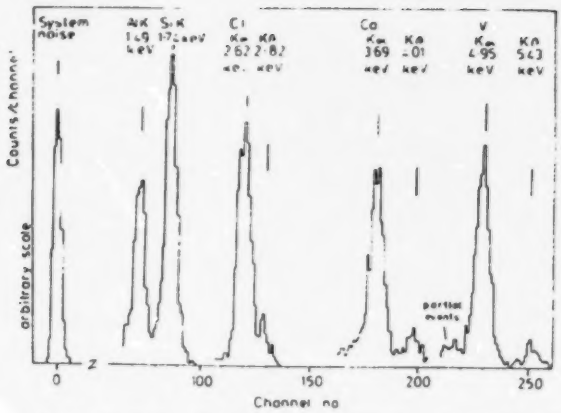

Fig. 7. Raw pulse height distributions for the P8600HR.

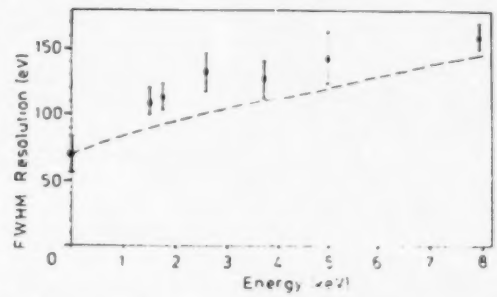

Fig. 8. Comparison of measured P8600HR energy resolution with predictions for 70 eV system resolution plus Fano factor statistics.

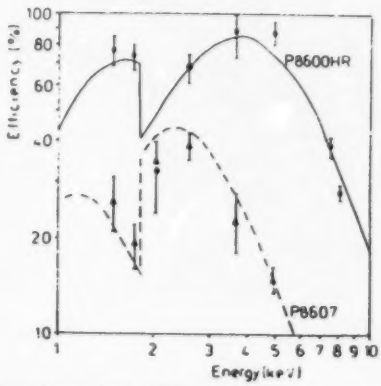

Fig. 9. Measured quantum efficiencies of P8607 (▲) and P8600HR (●) compared with the predictions for 3 μm (---) and 30 μm (——) depletion layers.

trons rms. Pixel readout rates were ~50 kHz, and frame times of ~1 to 100 s were used, depending on readout modes.

A fluorescent x-ray source was mounted within the CCD dewar with a number of targets that allowed tests with energies from 1.5 to 8 keV. Of particular importance was the variation of quantum efficiency with energy. The absolute x-ray count rates were calibrated with thin-windowed proportional counters of known geometry and gas absorption properties. Efficiency is defined here as the fraction of incident photons producing an event within the full-energy photopeak and contained within a single pixel.

The acceptance criterion for these data was determined empirically for each measurement from the point where the low-energy tail events merged with the peak in the pulse height distributions. This fractional pulse height value (h') varied with x-ray energy, due to the changing relative energy resolution, and with the fraction of events absorbed below the depletion layer.

Figure 5 illustrates the experimental arrangement employed for this work.

4. RESULTS

Figures 6 and 7 compare the raw pulse height distributions from the P8607 and P8600HR devices, respectively, for a number of monochromatic x-ray inputs. The FWHM resolutions of the P8607 are good, but the overall response is degraded by the partial events. The effect of partial events is much reduced in the case of the P8600HR. In Fig. 8, the P8600HR resolution is plotted as a function of energy and compared with the predictions for the measured system noise.

Figure 9 compares the measured quantum efficiencies of the P8607 and P8600HR with the predictions based on depletion depths of 3 μm and 30 μm, respectively, together with the transmission of the frontside electrode structure. Good

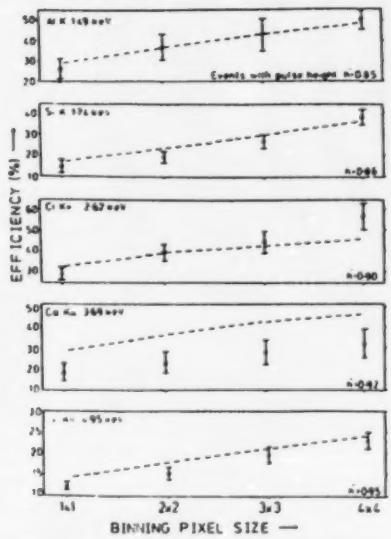

Fig. 10. Increase in efficiency with pixel size for the P8607.

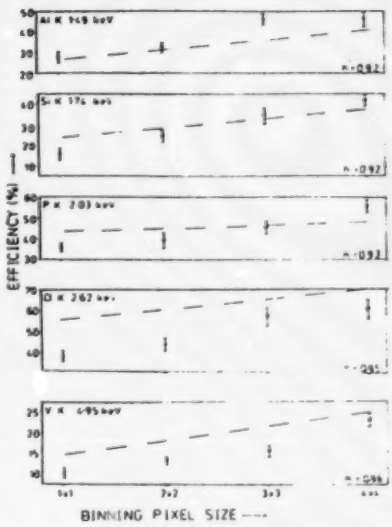

Fig. 11. Increase in efficiency with pixel size for the P8603.

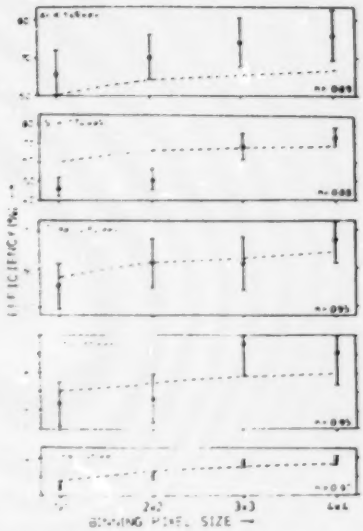

Fig. 12. Increase in efficiency with pixel size for the P8600HR.

agreement is demonstrated, and the expected increase in efficiency offered by high-resistivity silicon is confirmed.

Figures 10, 11, and 12 show the measured change in efficiency as a function of pixel size, together with the predictions of the models. Satisfactory agreement is apparent. There is a trend for the measured data to increase more rapidly than predicted. This is more apparent for the 2 to 3 keV data. In these cases, the silicon absorption coefficient is 0.5 μm^{-1}, and all photons are absorbed in the depletion layer. It is therefore thought that the discrepancy is due to the effects of the channel stops. In the channel stop regions there is a diminished field, and events are prone to splitting between pixels. As the pixels are binned the splitting is recovered, and the relative interpixel area liable to this effect is reduced.

5. DISCUSSION AND SUMMARY

The experimental data confirm the validity of the charge diffusion models adopted, although there are indications that the models would benefit from a more detailed account of the potential profiles, particularly in the channel stop regions. The effects of the diffusion within the field-free layers in standard CCDs are shown to degrade the attainable energy resolution. However, partial events are significantly reduced in the deep-depletion device, confirming that a fully depleted device should offer the ultimate energy resolution. In addition, the quantum efficiency is much improved, increasing the detection sensitivity of the CCD.

Conversely, these data show that x-ray tests may be a useful probe of the CCD structure. The injection of signals with well-determined absorption lengths allows the depths of different layers to be determined more precisely than with an optical input. This is due to the correspondence between pulse height of a single event and absorption depth. Single optical photons are not detectable, and no such correspondence can be deduced.

The use of thicker depletion layers allows for more efficient recognition of charged particle events. For example, minimum ionizing events deposit a peak of 80 electrons per micrometer of track. Therefore, a 40-μm-thick device would exhibit a response with an energy equivalent peak of 11 to 12 keV, which is above the upper energy threshold of the x-ray band. Furthermore, for a given angle of incidence of a particle, a deeper detection layer increases the probability of tracks extending to more than one pixel.

For enhanced soft x-ray response (<1 keV), back-illuminated CCDs may produce the highest efficiency, with dead layers in the range of tens of angstroms being attainable.[7] In x-ray astronomy applications, a filter is required to prevent optical photons from contaminating the x-ray measurements, but typical filters, for example, 1000 Å aluminum on a 2000 Å plastic base, also absorb low-energy x-ray photons. In a 40-μm-thick back-illuminated device, charge packets generated near the surface suffer 3 to 4 μm of radial diffusion before collection. Quantum efficiency is therefore affected by splitting of events between pixels. A careful trade-off must be made to assess such practical limits before a CCD is designed for a particular application.

It may be recalled that the resolution of the XMM optics is much worse than for AXAF, and therefore optical photons are more widely dispersed in the focal plane. The attenuation required to eliminate a significant background optical signal in each CCD pixel is therefore much lower, with the promise of higher sensitivity to sub-keV photons. This, together with a requirement for a wide bandwidth, indicates that back illumination is more suitable for XMM than for AXAF.

The lower spatial resolution also affects the choice of pixel size. Larger pixels tend to minimize the effects of charge splitting; however, this must be traded against other parameters such as achievable count rate per unit area, readout rate, and background rejection efficiency. It is probably better to design a CCD with a conventional 20 μm size, and where necessary bin up pixels on-chip to attain the required pixel dimensions. The complicated trade-offs involved in the choice of pixel size might vary from one observation to the next as the importance of the different scientific parameters changes.

The ability to specify different readout formats would preserve a greater degree of flexibility.

Clearly, there is no identifiable single CCD design that maximizes all x-ray performance parameters. Individual experiments may need different depletion depths and pixel sizes or may determine a preference for front or back illumination. We are currently embarking on a program with EEV to produce and test devices with thicker depletion layers, and these will be thinned to leave different amounts of field-free substrate. Eventually, a fully depleted device would be produced to allow front or back illumination. This range of CCDs would be tested to determine the x-ray energy resolutions, detection efficiencies, and background rejection capabilities in order to establish the optimum design for the XMM program.

6. ACKNOWLEDGMENTS

The help and advice provided by D. J. Burt of the GEC Hirst Research Centre and P. C. Bailey of EEV Ltd. are gratefully acknowledged. E. G. Chowanietz is a recipient of a Science and Engineering Council Co-operative Award in Science and Engineering studentship.

7. REFERENCES

1. G. P. Garmire et al., "The AXAF CCD imaging spectrometer," in *X-Ray Instrumentation in Astronomy*, J. L. Culhane, ed., Proc. SPIE 597, 261-266 (1986).
2. An ESA workshop on a cosmic x-ray spectroscopy mission (Lyngby, Denmark), European Space Agency, SP-239, Noordwijk, The Netherlands (1985).
3. R. Giacconi et al., "The Einstein (HEAO 2) X-ray Observatory," Astrophys. J. 230, 540 (1979).
4. J. R. Janesick, T. Elliott, S. Collins, T. Daud, D. Campbell, A. Dingizian, and G. P. Garmire, "CCD advances for x-ray scientific measurements in 1985," in *X-Ray Instrumentation in Astronomy*, J. L. Culhane, ed., Proc. SPIE 597, 364-380 (1986).
5. G. R. Hopkinson, "Charge diffusion effects in CCD x-ray detectors—I: theory," Nucl. Instrum. Methods Phys. Res. 216, 423 (1983).
6. G. R. Hopkinson, "Analytic modeling of charge diffusion in charge-coupled device imagers," Opt. Eng. 26(8), (1987).
7. J. R. Janesick, T. Elliott, T. Daud, and D. Campbell, "The CCD flash gate," in *Instrumentation in Astronomy VI*, D. L. Crawford, ed., Proc. SPIE 627, 543-582 (1986).

David H. Lumb received the B.Sc. and M.Sc. degrees from Leicester University in 1978 and 1980, respectively. In 1979 he joined the X-ray Astronomy Group at Leicester to study the use of CCDs for x-ray imaging spectroscopy, and in 1983 he received the Ph.D. degree. He was a visiting scientist at the Harvard Center for Astrophysics/Smithsonian Astrophysical Observatory in 1984/85, and currently he is studying the optimization of CCD response to allow implementation on future spaceborne observatories.

Eric G. Chowanietz received the B.Sc. degree from Lanchester Polytechnic in 1983. He was a research student at Leicester University until 1986, studying CCD enhancements for x-ray measurements, and in 1987 he received the Ph.D. degree.

Alan A. Wells received the B.Sc. degree in applied physics from City University of London in 1962 and the M.Sc. degree in plasma physics from the University of London in 1966. He is currently Principal Research Fellow and Manager of Space Projects, Department of Physics, University of Leicester, and has worked on the Ariel 5, Ariel 6, EXOSAT, ASTRO-C, and Einstein satellites and on Skylark rocket experiments. He is also currently payload project scientist leading the UK consortium developing the wide field camera for ROSAT. From 1982 to 1985 he was joint project leader of the University of Leicester/GEC/EEV Cooperative Research Program to develop x-ray CCDs. He has 25 publications to his credit.

Charge-coupled device advances for x-ray scientific applications in 1986

James R. Janesick
Tom Elliott
Stewart Collins, MEMBER SPIE
Taher Daud, MEMBER SPIE
Dave Campbell, MEMBER SPIE
Jet Propulsion Laboratory
California Institute of Technology
4800 Oak Grove Drive
Pasadena, California 91109

Gordon Garmire
Pennsylvania State University
525 Davey Laboratory
University Park, Pennsylvania 16802

Abstract. A theoretical model is presented that predicts the output response of a thinned CCD to soft x-ray spectra. The model simulates the four fundamental parameters that ultimately limit CCD performance: quantum efficiency, charge collection efficiency, charge transfer efficiency, and read noise. Simulated results are presented for a wide variety of CCD structures, and general conclusions are presented about achieving a practical balance of sensitivity, energy, and spatial resolution for an Advanced X-ray Astrophysics Facility (AXAF) instrument. We compare the results of the analysis to existing state-of-the-art CCDs and project improvements that will be made in the near future.

Subject terms: x-ray CCDs; imaging x-ray spectrometer; Advanced X-ray Astrophysics Facility (AXAF); backside/frontside illumination; charge diffusion; detector quantum efficiency; charge transfer efficiency; read noise; charge collection efficiency.

Optical Engineering 26(2), 156-166 (February 1987).

CONTENTS

1. Introduction
2. The CCD
3. X-ray model
   3.1. Photon absorption
   3.2. Initial cloud diameter
   3.3. Field-free region
   3.4. Field region
   3.5. Final cloud diameter
   3.6. Charge splitting
4. X-ray model results
5. Charge transfer loss
   5.1. Proportional transfer loss
   5.2. Fixed transfer loss
6. Experimental data
7. Conclusions
8. Acknowledgments
9. References

1. INTRODUCTION

For approximately five years the Jet Propulsion Laboratory, the Pennsylvania State University, and the Massachusetts Institute of Technology have collaborated on a program to develop and utilize charge-coupled devices (CCDs) to obtain energy-resolved images of astronomical sources in the x-ray region of the spectrum. The three institutions are now engaged in defining the Advanced X-ray Astrophysics Facility (AXAF) CCD Imaging Spectrometer (ACIS), a CCD-based instrument tentatively selected by NASA for use on the AXAF observatory.[1] Initial results of the CCD development and evaluation have been reported,[2-4] and our Black Brandt sounding rocket x-ray CCD imaging spectrometer is scheduled for its first flight late in 1987.

This paper reports preliminary results of an effort to accurately model the x-ray performance of prospective AXAF CCDs. X-ray imaging spectroscopy places demands upon CCD performance that differ from (and are usually more stringent than) the demands of other applications. Further, there now exist a wider variety of CCD structures to choose from: virtual phase[5] or multiphase,[6] thick or thin, front- or backside-illuminated, etc. Developing and testing such a spectrum of devices would require prohibitive amounts of time and money, so it is important that suitable analytical techniques be developed to permit such evaluation. While the characteristics of some trade-offs are clear, a few questions have not received adequate attention to quantitatively assess their implications. For example, the diffusion of photogenerated charge into more than one pixel is found to have a significant impact on the energy-resolving capability of a CCD and on data reduction algorithms. In this paper, a theoretical model of such diffusion is developed. This model permits the synthesis of x-ray spectra for a wide variety of thinned CCD structures, thereby permitting the selection of properties that yield an optimum balance of sensitivity and energy resolution. At the conclusion of this paper, a few experimental results are provided that support the validity of the model for existing devices.

2. THE CCD

The fundamental parameters that ultimately limit CCD performance are (1) read noise, (2) charge transfer efficiency (CTE), (3) quantum efficiency (QE), and (4) charge collection efficiency (CCE).

At the present stage of their development, it is possible to fabricate devices that have low read noise (in the 4 to 15 e^- range), excellent CTE performance (>0.99999), and high QE performance over the entire spectral range, 1 to 11,000 Å.[7] As impressive as these performance parameters are, the full potential of CCE lies well beyond that which is typically realized in currently available devices. During the past two years JPL has been optimizing CCE performance of the CCD for use in x-ray spectrometer applications. CCE is the parameter that measures the ability of the CCD to collect all signal charge generated from a single photon event into a single pixel. High CCE performance is especially critical to

Paper 2252 received Dec. 2, 1985; revised manuscript received Oct. 24, 1986; accepted for publication Oct. 24, 1986; received by Managing Editor Nov. 3, 1986. This paper is a revision of Paper 597-42 which was presented at the SPIE conference on X-Ray Instrumentation in Astronomy, Dec. 2-4, 1985, Cannes, France. The paper presented there appears (unrefereed) in SPIE Proceedings Vol. 597.
© 1987 Society of Photo-Optical Instrumentation Engineers.

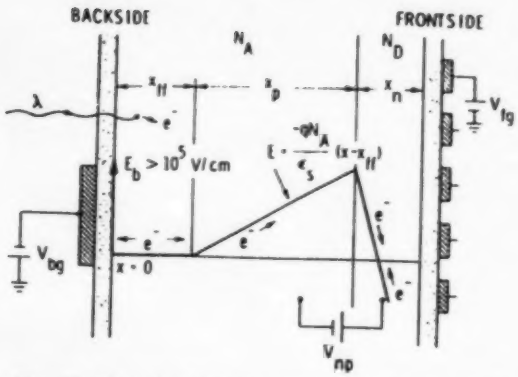

Fig. 1. Cross section of the CCD configuration to be analyzed in this paper showing the field-free region x_{ff}, the p-depletion region x_p with acceptor concentration N_A, and the n-depletion region x_n with donor concentration N_D. The electric field within x_p and x_n is generated through the voltages V_{np} and V_{bg}. The backside reflecting field E_b is provided by voltage V_{bg}. Backside illumination is illustrated. Frontside illumination is also possible and is advantageous in some applications.

soft x-ray applications, where the ability of the CCD to accurately determine the energy of the photon depends upon collecting all of the photogenerated charge properly. Experience has shown that complete charge collection requires that two criteria be met: (1) there must be no trapping centers within the CCD that cause signal charge to be lost by recombination, and (2) the charge produced by an individual photon must be collected within a single pixel and must not be allowed to divide among several pixels. Charge loss causes the photon energy to be underestimated. Charge splitting degrades the precision of charge measurement by requiring the summation of several noisy pixels.

The degree of charge loss and charge splitting depends upon where in the pixel the photon is absorbed. Photons absorbed within the frontside depletion region (see Fig. 1) of a given pixel are typically seen as the ideal event and are called "single pixel events." Photons absorbed deeper in the depletion region, where the electric field is weaker, or below the depletion region, in the field-free area of the CCD, create a charge cloud that thermally diffuses outward until reaching the sharply defined potential wells at the lower boundary of the pixel array. At that point, the charge cloud may split into two or more packets, which are collected in adjacent pixels. Events of this type are called "split events." Events where charge is not conserved are called simply "partial events" and are usually generated in regions deep within the CCD where loss of carriers through recombination occurs (currently common to the thick frontside-illuminated CCD).[8]

At this time in the development of the CCD, the thinned CCD is superior to the thick CCD in achieving high CCE performance. This is because the thinned device allows field control over most of the photosensitive volume, which eliminates both the neutral bulk and the trapping centers where photogenerated charge can diffuse and recombine to produce partial and split events. A cross section through the signal channel of the thinned CCD (shown backside-illuminated) is schematically represented in Fig. 1. Such a structure has been experimentally tested and found to yield both 100% internal quantum efficiency (i.e., no partial events) and the highest CCE performance to date (i.e., very few split events) due to charge diffusion.

The thinned CCD relies on three bias voltages (shown in Fig. 1) to establish the proper electric field conditions throughout the photosensitive volume: V_{bg} = backside gate voltage, V_{np} = frontside depletion voltage, and V_{fg} = frontside gate voltage. The backside gate voltage, V_{bg}, is required to form an accumulation layer on the backside of the CCD to drive photoelectrons generated near the backside to the frontside potential well. The accumulation layer must be sufficient to create a field greater than 10^5 V/cm at the back surface to prevent signal carriers from diffusing to that surface and being lost to recombination. It has been shown experimentally that such fields can be achieved either by the technique of backside charging[9] or by the flash gate.[10]

The frontside depletion voltage, V_{np}, in conjunction with the frontside gate voltage, V_{fg}, is used to control the electric field within the CCD channel. During the integration of signal charge, both V_{np} and V_{fg} are adjusted to eliminate the field-free region x_{ff} (shown in Fig. 1) by forcing the frontside depletion region to meet the backside accumulation region. The maximum depth (depending on V_{fg}) that the p-depletion region, x_p, extends toward the backside can be calculated from[10]

$$x_p \simeq \left[\frac{2\epsilon_S N_D}{qN_A(N_A+N_D)}\,(V_{bi}+V_{np})\right]^{1/2}. \qquad (1)$$

where ϵ_S is the permittivity of silicon (1.044×10^{-12} F/cm), N_D is the donor concentration of the n-channel (1.5×10^{16} cm^{-3}), N_A is the acceptor concentration of the p-region (cm^{-3}), q is electronic charge (1.6×10^{-19} C), V_{bi} is the built-in potential ($\simeq 0.6$ V), and V_{np} is the potential of the CCD channel relative to the substrate.

Under proper bias conditions, an electric field can exist throughout the entire CCD channel (from front to back), which directs signal carriers to the CCD potential well with minimal charge diffusion. The electric field within the p-depletion region as a function of $(x - x_{ff})$ is given by

$$E(x) \simeq \frac{-qN_A(x-x_{ff})}{\epsilon_S} \quad \text{for } x_{ff} < x < x_p + x_{ff}. \qquad (2)$$

3. X-RAY MODEL

The CCD structure shown in Fig. 1 lends itself to use of a relatively simple Monte Carlo computer simulation to analyze x-ray absorption and charge collection processes for different CCD parameters and input x-ray spectra. Specifically, we use the model to determine the number of split events generated for the backside and frontside-illuminated CCD as a function of field-free distance x_{ff}, acceptor concentration N_A, pixel size P_s, and x-ray energy E_λ, over the range 0.1 to 10 keV. The computer model first simulates photon absorption and generation of charge. It then follows each photoelectron generated by the x-ray event as it moves within the CCD and keeps track of the overall electron cloud distribution as its diameter (two sigma) grows by diffusion until it reaches the CCD potential well. The amount of charge that splits among pixels is determined by the fraction of the electron cloud distribution within each pixel's lateral boundaries. The model also includes the effects of read noise and charge transfer efficiency. A read noise of 10 electrons (one sigma) is assumed for all simulations in this paper. Charge transfer effects are included in Sec. 5.

3.1. Photon absorption

The computer program begins by simulating (1) photon absorption and (2) generation of charge, where the number of photons absorbed at a distance x_s into the backside of the CCD varies as $\exp(-\alpha x_s)$. The absorption coefficient $\alpha(cm^{-1})$ as a function of photon energy E_λ can be found with the following set of equations covering an energy range from 0.1 to 10 keV:

$$\alpha \simeq 2.42[(2.4935\times10^5) - (1.147\times10^6 E_\lambda) - (3.152\times10^6 E_\lambda^2) + (2.2349\times10^7 E_\lambda^3)], \quad \text{for } 0.1 < E_\lambda \le 0.154 . \tag{3}$$

$$\alpha \simeq 2.42\times10^{[3.1867 - 2.707\mathrm{Log}(E_\lambda) + 0.07554[\mathrm{Log}(E_\lambda)]^2 + 0.8729[\mathrm{Log}(E_\lambda)]^3]}, \quad \text{for } 0.154 < E_\lambda \le 1.78 . \tag{4}$$

$$\alpha \simeq 2.42\times10^{[-2.78\mathrm{Log}(E_\lambda) + 4.3]} \quad \text{for } 1.78 < E_\lambda < 10 . \tag{5}$$

3.2. Initial cloud diameter

During photon absorption, the photon imparts its energy to an inner shell electron of a silicon atom in the lattice, which in turn excites a chain of outer shell electrons in nearby atoms through a series of quasi-elastic Rutherford scattering collisions. Most of the dissipated energy generates electron hole pairs. By analogy with high energy electron beam interaction with silicon, one can approximate the energy/depth relationship as $R = KE_\lambda^n$, where K and n are numerical constants for the material and R is the penetration depth. The electron-hole-pair creation zone can be approximated as a sphere, centered at the absorption depth of the impinging photon, with C_i (cm) as its diameter. For silicon C_i is given by[11]

$$C_i \simeq 0.0171(E_\lambda)^{1.75}\times10^{-4} . \tag{6}$$

Figure 2 plots C_i as a function of photon energy and shows that the initial cloud diameter grows rapidly with energy, obtaining a diameter of almost 1 μm at 10 keV.

3.3. Field-free region

For an x-ray event generated within the field-free region x_{ff}, the computer simulation allows each photoelectron to randomly wander around, as demonstrated in Fig. 3 (shown using $x_s = 0$). If the electron reaches the backside by the random walk, the backside field E_b will reflect it toward the frontside to wander within x_{ff} again. The process continues until the electron reaches the edge of the p-depletion region, at which point its lateral dimension from the point of generation is measured and stored in computer memory and used later to statistically determine the two-sigma event cloud diameter C_{ff}.

Figure 4 presents the results of a 2 h computer run generated under the conditions discussed above for 2000 photon events per given x_s. The figure plots the cloud diameter as a function of x_s for field-free region thicknesses of 0.05, 0.1, and 0.2 μm. An equation that empirically fits these data points and describes the cloud diameter C_{ff} as a function of x_{ff} and x_s is given by

$$C_{ff} \simeq 2x_{ff}\left[1 - \left(\frac{x_s}{x_{ff}}\right)^2\right]^{1/2} \quad \text{for } 0 < x_s < x_{ff} . \tag{7}$$

Note from Eq. (7) that the worst case situation (i.e., that which produces the largest cloud diameter within the field-free region) occurs when the photon is absorbed at the back surface (i.e., $x_s = 0$; $C_{ff} = 2.0x_{ff}$). For example, a photon that interacts at the surface with a field-free region 5 μm deep will produce a 10 μm cloud diameter at the p-depletion edge (neglecting the initial cloud diameter C_i).

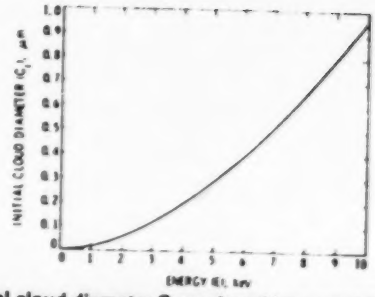

Fig. 2. Initial cloud diameter C_i produced immediately after photon absorption as a function of its energy.

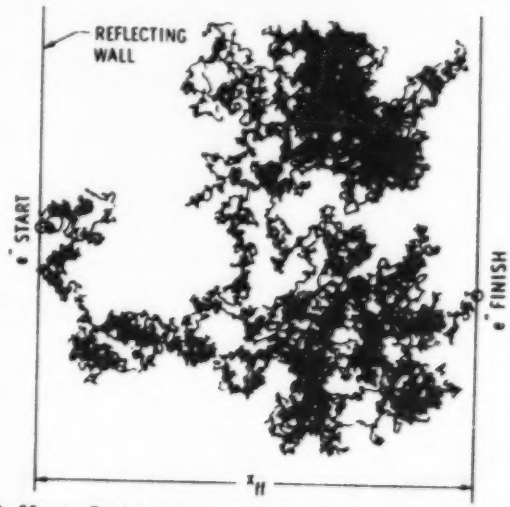

Fig. 3. Monte Carlo random walk of a photoelectron generated at the backside (i.e., $x_s = 0$) within the field-free region x_{ff}. The reflecting wall at the backside is provided by the electric field E_b, which forces the electron to the p-depletion edge, where it is eventually swept to a CCD potential well at the frontside.

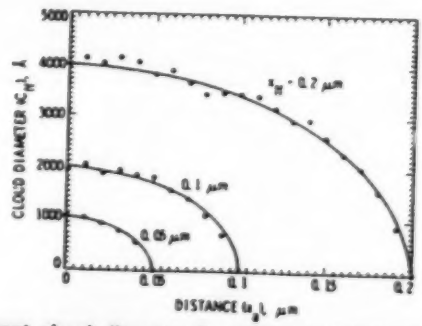

Fig. 4. Event cloud diameter C_{ff} generated within the field-free region x_{ff}, measured at the p-depletion edge as a function of photon absorption depth x_s. Each data point is statistically derived from 2000 individual random walk experiments, as demonstrated in Fig. 3 for each x_s. The solid lines are plots of Eq. (7), showing that the random process can be described analytically.

It should be mentioned that the behavior shown in Fig. 4 is independent of the electron's mean free path; that is, the Monte Carlo simulation results are the same no matter what path length is chosen for each random step in the random walk.

3.4. Field region

For an x-ray event that occurs in the field region x_p, the simulated photoelectron also wanders randomly, as in the field-free case, except that a drift component of distance $\mu E \bar{x}/v_{th}$ in the direction of the CCD potential well is added to each random step, where μ is the electron mobility (1350 $cm^2 \cdot V^{-1} \cdot s^{-1}$), E is the electric field within the p-depletion region x_p [Eq. (2)], $\bar{x}$ is the mean free path of the electron under diffusion (typically 60 Å), and v_{th} is the electron's thermal velocity (10^7 cm/s). The photoelectron wanders and drifts until it reaches the n-p junction, where its lateral displacement is measured from the point of generation and is used to determine the two-sigma event cloud diameter, C_f.

Under the conditions discussed above, the cloud diameter within the field region behalves, as shown in Fig. 5, as a function of distance $(x_a - x_{ff})$ into the field region for doping concentrations of 10^{15} and 10^{16} cm^{-3}. An equation that empirically fits these data points and describes the cloud diameter C_f as a function of $(x_a - x_{ff})$ and N_A is given by

$$C_f \simeq \left\{ -2 \left[5.1 \times 10^{-6} \left(\frac{10^{15}}{N_A} \right)^{1.2} \right]^2 \ln \left(\frac{x_a - x_{ff}}{x_p} \right) \right\}^{1.2} . \tag{8}$$

$$C_f(\max) \simeq 1.85 \times 10^{-5} \left(\frac{10^{15}}{N_A} \right)^{1/2} \quad \text{for } x_{ff} \leqq x_a \leqq x_p + x_{ff} .$$

Equation (8) and Fig. 5 show that the cloud diameter grows to an appreciable size for photon absorption near the p-depletion edge. Also, the cloud diameter increases with decreasing N_A because the depletion region becomes physically larger [Eq. (1)] and the electric field within this region decreases [Eq. (2)]. Both these factors permit more diffusion to occur, which produces a larger cloud size at the n-p junction.

3.5. Final cloud diameter

The final cloud diameter for an event that experiences both the field-free and field regions can be approximated by the quadrature sum of the individual cloud diameters,

$$C_D \simeq (C_i^2 + C_{ff}^2 + C_f^2)^{1/2} . \tag{9}$$

As shown next, the final cloud diameter for low energy x-rays (where absorption takes place near the backside) will be essentially determined by diffusion processes within x_{ff} and x_p, with the initial cloud diameter being negligibly small. However, for higher energies, absorption takes place deeper in the CCD, where the electric field is stronger and the amount of diffusion is small compared to the initial cloud diameter.

3.6. Charge splitting

In our computer model we assume that an event cloud reaching the n-p junction has a two-dimensional Gaussian distribution of charge given by

$$Q_i \simeq \frac{E_A}{3.65} \frac{1}{2\pi\sigma^2} \exp \left\{ - \left[\frac{(x - m_x)^2 + (y - m_y)^2}{2\sigma^2} \right] \right\} . \tag{10}$$

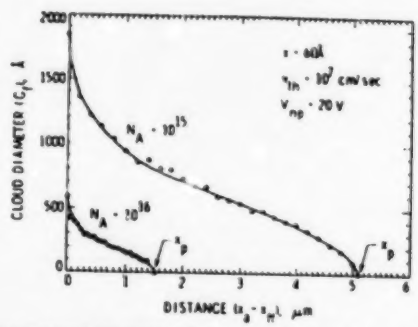

Fig. 5. Event cloud diameter C_f generated within the field region x_p, measured at the n-p junction as a function of photon absorption depth $(x_a - x_{ff})$. Each data point is derived from 10,000 individual random walk experiments under the field conditions described by Eq. (2). The solid lines represent an approximation to the random process given by Eq. (8).

where m_x and m_y, the coordinates of the center of the event cloud, randomly vary between 0 and 1 within a pixel of 1×1 dimension (i.e., when $m_x = 0.5$ and $m_y = 0.5$ the center of the cloud is at the center of the pixel). The sigma σ given in Eq. (10) is related to actual pixel size P_s (cm) and final cloud diameter C_D at the n-p junction through the equation

$$\sigma \simeq \frac{C_D}{2P_s} . \tag{11}$$

The number of electrons collected by the primary pixel (the pixel where the photon is incident) is the fraction of the electron cloud distribution given by Eq. (10) found within the pixel's lateral boundaries, which can be found through the equation

$$Q_p \simeq \frac{E_A}{3.65} \left\{ P\left(\frac{1 - m_x}{\sigma} \right) - \left[1 - P\left(\frac{m_x}{\sigma} \right) \right] \right\} \left\{ P\left(\frac{1 - m_y}{\sigma} \right) - \left[1 - P\left(\frac{m_y}{\sigma} \right) \right] \right\} , \tag{12}$$

where

$$P(t) \simeq 1 - 0.5(1 + 0.196754t + 0.115194t^2 + 0.000344t^3 + 0.019527t^4)^{-4} . \tag{13}$$

The amount of charge within the adjacent pixel (the split portion) is given simply by

$$Q_s \simeq \left(\frac{E_A}{3.65} \right) - Q_p . \tag{14}$$

In our model an event is assumed to be split when $Q_s > 0.01 Q_p$. Also, it is assumed that no more than two pixels are involved when an x-ray event is generated, a condition that is true only when the cloud diameter is much smaller than the pixel size. Experimentally we find very few events occupying more than two pixels for the fully depleted thinned CCD, and therefore for our computer simulation we assume that only two pixels are involved per split event.

TABLE I. CCD structures simulated in this paper whose characteristics differ by acceptor concentration N_A, field thickness $x_p + x_n$, field-free thickness x_H, type of illumination, and pixel size.

Structure	N_A(cm^{-3})	$x_p + x_n$(μm)	x_H(μm)	Illumination	Pixel size (μm)
A	10^{15}	6	0	backside	15
B	10^{13}	51	0	backside	15
C	10^{15}	6	2	backside	15
D	10^{13}	51	2	backside	15
E	10^{15}	6	0	backside	60
F	10^{13}	51	0	backside	60
G	10^{15}	6	0	frontside	15
H	10^{13}	51	0	frontside	15

4. X-RAY MODEL RESULTS

The model described in the preceding section includes a number of variables, among which are the following:

(a) epiresistivity (directly implying acceptor concentration and depletion depth);
(b) thickness of field-free layer, if present;
(c) energy absorption profile (depends on photon energy and direction of illumination; front or backside); and
(d) pixel size.

We have simulated the x-ray performance of a variety of hypothetical CCD structures whose characteristics are listed in Table I. None of these structures is "optimum" in its x-ray performance. Rather, these structures have been chosen because they span interesting ranges of conditions and serve to illustrate the sensitivity of performance to reasonable variations in structure. Structure A is unique in that it corresponds closely to an existing CCD structure (the thinned Texas Instruments 800×800 three-phase CCD,[6,7] TI 3PCCD) and therefore yields results that can be compared directly to experimental data.

Although the structures differ from one another in the parameters listed in Table I, they all are assumed to have a read noise floor of 10 electrons (one sigma) and no loss of signal charge at the back surface (i.e., 100% internal quantum efficiency). This latter assumption is found to be valid for CCDs for which the substrate has been completely removed and backside accumulated. It is not valid for the unthinned devices we have tested, although it may yet be possible to fabricate an unthinned CCD whose substrate and epi layers are effectively isolated from one another.

Figure 6 compares the performance of structures A and B, which differ only in thickness and resistivity. As expected, the higher resistivity, thicker device ($N_A = 10^{13}$, $x_p + x_n = 51$ μm) provides significantly greater sensitivity (especially at high energies) than does the thin, low resistivity structure. However, the frequency of charge splitting is also much greater for the thick CCD by a factor that varies between 1.5 and 8 as a function of energy. In fact, for a given incident flux of x rays, the thick CCD (structure B) provides a greater quantity of nonsplit events only at energies greater than about 4.5 keV. Below this energy, the thin detector outperforms the thick one by a substantial margin.

Figure 7 illustrates the effects of a field-free layer by simulating CCDs whose thicknesses are 2 μm greater than their depletion depth (structures C and D). For the thin device, the additional thickness provides a slight increase in sensitivity throughout the range of approximately 2 to 10 keV while also significantly increasing the occurrence of charge splitting at low energies. For the thick device, charge splitting also substantially increases below 5 keV with a negligible change in sensitivity because the 2 μm represents a smaller fraction of the initial device thickness.

Figure 8 (structures E and F) illustrates the effect of increasing the pixel size, which dramatically reduces the frequency of charge splitting while preserving the initial quantum efficiency (again compare with Fig. 6).

Finally, Fig. 9 illustrates the performance of a thinned frontside-illuminated CCD (structures G and H), a device that substantially reduces the conflict between sensitivity and

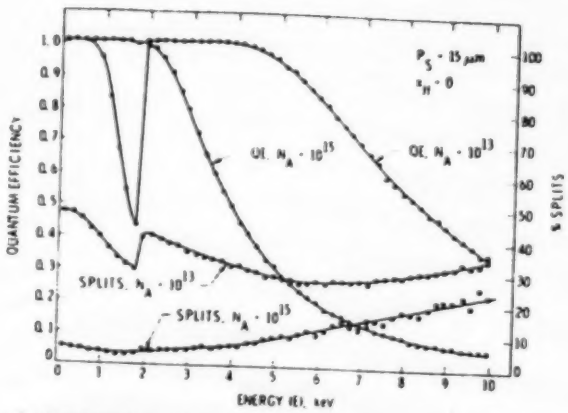

Fig. 6. Predicted quantum efficiency and frequency of charge splitting are shown for structures A and B of Table I. Quantum efficiency is for device thicknesses of 6 μm and 51 μm, respectively ($x_p + x_n$). Split event frequency is based on Eqs. (12) and (14). A split event is defined as one for which 1% of the initial charge is lost from the primary pixel. The frequency of split events is higher at both high and low energy than at the intermediate minimum. At lowest energies, photons are absorbed predominately at the back surface, allowing for charge diffusion prior to collection in the frontside potential wells. This is particularly severe for the thick device. At high energies, the initial electron cloud is large enough to provide a significant probability of charge splitting without subsequent diffusion.

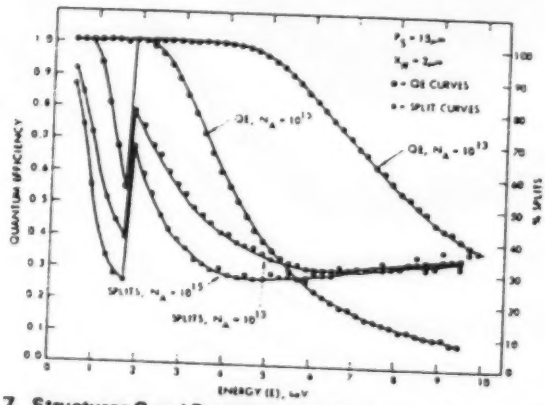

Fig. 7. Structures C and D compared in the manner shown in Fig. 6. The addition of a 2-μm layer of field-free material to structure A ($N_A = 10^{15}$) results in a slight increase in high energy sensitivity and a significant increase in low energy charge splitting. Its effect on the thick device (structure B) is similar except that the sensitivity increase is much less.

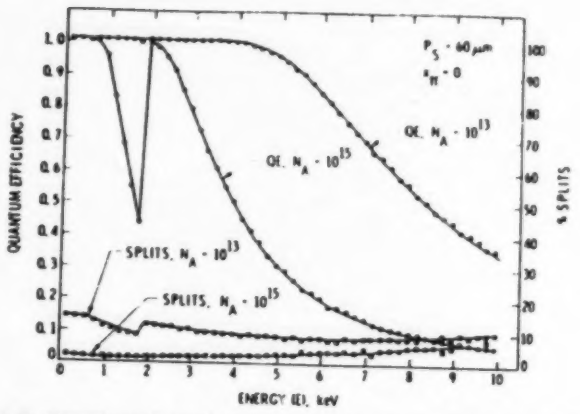

Fig. 8. Structures E and F compared in the manner of Figs. 6 and 7. The use of larger pixels (60 μm) dramatically reduces the frequency of split events for both cases.

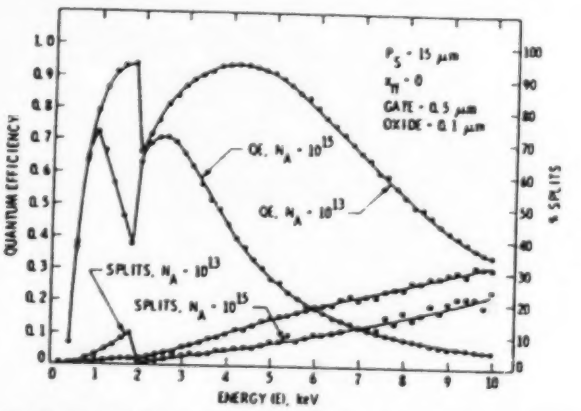

Fig. 9. Structures G and H compared in the manner of Figs. 6 to 8. For this comparison of thinned frontside-illuminated devices, it is assumed that the front surface is overlaid with 1000 Å of gate oxide and 5000 Å polysilicon gates. At energies greater than 1 keV, these devices have sensitivity comparable to the backside-illuminated cases, with substantially fewer split events at all energies.

charge splitting. Although frontside sensitivity is relatively poor at low energies (< 1 keV) due to photon absorption by overlying oxide and gate layers, the effect of this loss may not be significant in many applications. In an actual x-ray CCD instrument, for example, it is necessary to utilize a filter material such as aluminum to attenuate contaminating non-x-ray illumination (i.e., UV, visible, and infrared radiation). Inevitably, this filter dramatically reduces the low energy flux to the CCD to a level far below that of a bare device. As before, split events are greater for the thick device, but with frontside illumination the frequency of splitting is lower than for backside illumination, with the greatest improvement occurring at low energies. This result is due to the fact that, with frontside illumination, the greatest amount of charge is always generated near the front surface, where the field strength is greatest.

While Figs. 6 to 9 define the various trade-offs represented in Table I, they give no "feel" for how these properties would affect x-ray spectra. Figures 10 to 13 provide such a comparison for a hypothetical input spectrum consisting of a series of narrow lines spaced at 500-eV intervals, each containing the same number of photons. Figures 14 to 16 illustrate the more realistic example of an astronomical target, Her. X-1. Each set of examples shows how, for backside illumination, increased thickness and improved high energy performance yield a substantial quantity of split events, which manifest themselves as an increased spectral background level at low energies. In general, it appears that adding field-free thickness to the backside is a poor choice, for it does little to enhance the strength of spectral features while adding considerably to the incidence of split events, which complicate the identification and measurement of low energy features (see Figs. 14 and 15). The use of thicker, field-free devices is less clear (Fig. 16). For the backside illumination, this yields improved performance at high energies and degraded performance at low energies. As a final note on charge splitting, we point out that data reduction software can identify split events and sum the signal from the affected pixels. However, we have found that this always broadens spectral features and typically displaces them toward lower energies. Clearly, additional work in this area is warranted.

5. CHARGE TRANSFER LOSS

Up to this point we have assumed perfect charge transfer efficiency for the CCD. In this section we include charge transfer loss, which completes the model in simulating all four fundamental parameters that limit CCD performance, as discussed in Sec. 2.

The total amount of charge in an x-ray event is usually conserved during transfer through the CCD. Transfer loss is typically referred to as the redistribution of charge from the primary pixel into trailing pixels. In practical CCDs, transfer loss is best described as a combination of a fractional loss and an additional fixed loss of charge.[12] Fractional loss is proportional to the size of the charge packet. Fixed loss is independent of the size of the charge packet. Both loss mechanisms can normally be eliminated by the use of a bias or fat-zero charge at the sacrifice of increasing read noise.

5.1. Proportional transfer loss

It can be shown that the response to an x-ray event for a CCD with proportional loss can be approximated in a given transfer direction by

$$Q_1 \simeq Q_{p-a} \exp(-N\epsilon) ,$$
$$Q_n \simeq Q_{p-a} \frac{(N\epsilon)^{(n-1)}}{(n-1)!} \exp(-N\epsilon) , \quad n = 2,3,4,\ldots , \tag{15}$$

where Q_{p-a} represents the charge within the primary (or adjacent) pixel before charge transfer, Q_1 is the amount of charge remaining in the primary (or adjacent) pixel after transfer, N is the number of pixels transferred (vertically or horizontally), ϵ is the charge transfer inefficiency per transfer due to proportional loss, and Q_n is the quantity of charge found in the $(n-1)th$ trailing pixel.

The use of Eq. (15) in conjunction with the Monte Carlo simulation discussed above can demonstrate the effects of proportional loss on CCD performance. Figure 17 shows the expected performance of a 100×100 pixel CCD array uniformly illuminated under the same conditions used in generating Fig. 10 and assuming a CTE of 0.9999 (CTE $= 1 - \epsilon$) for both vertical and horizontal transfer directions. A slight degradation in performance is observed when comparing these figures in that the higher energy lines in Fig. 17 are shifted

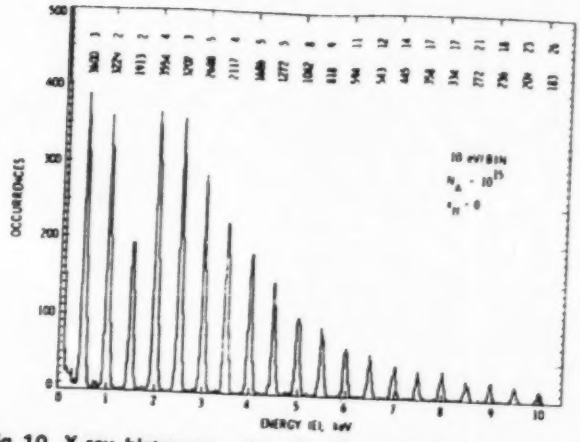

Fig. 10. X-ray histogram using the Monte Carlo simulation discussed in Sec. 3. The input spectrum to the CCD is a series of lines (3600 photons/line) spaced at 500-eV intervals. The numbers at the top of the figures indicate the total number of photons absorbed by the CCD (out of 3600) and the percentage of split events generated of those photons that are absorbed. Structure A is shown in this figure.

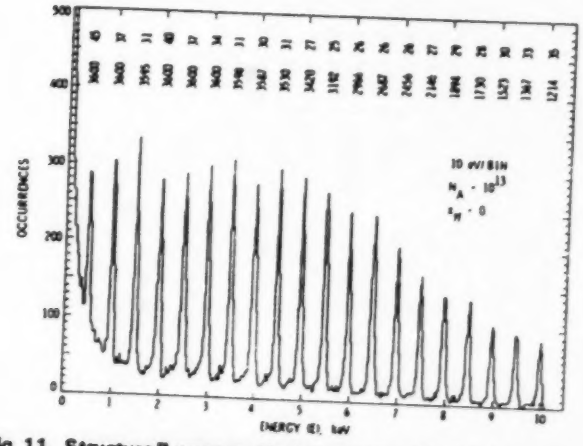

Fig. 11. Structure B presented in the manner of Fig. 10. The increase in split events is due to a thicker epilayer and appears in this figure as an increased background level between the low energy lines.

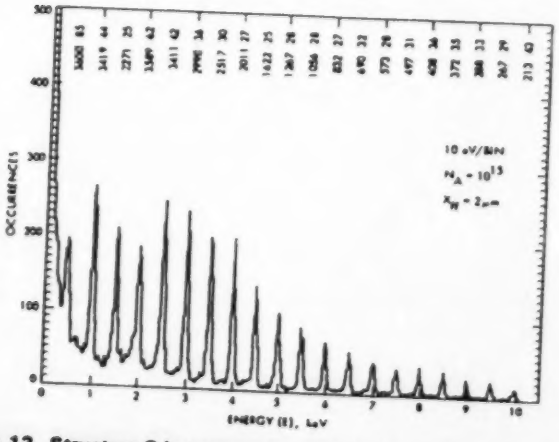

Fig. 12. Structure C is presented in the manner of Figs. 10 and 11. The addition of a field-free layer serves to increase the occurrence of charge splitting relative to the example shown in Fig. 10.

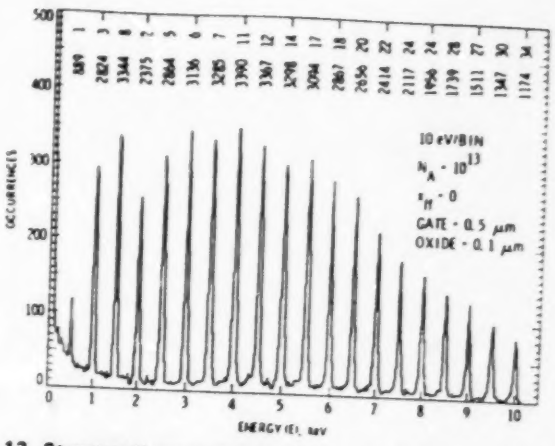

Fig. 13. Structure H presented in the manner of Figs. 10 to 12. A substantial reduction in split events is shown relative to the backside-illuminated, thick device of Fig. 11.

downward slightly owing to transfer loss. However, when the same CTE factor is used to simulate the effects of transfer loss for a 2000×2000 pixel CCD, the higher energy lines suffer severely, as shown in Fig. 18. In Figs. 19 and 20, the same 2000×2000 CCD is simulated, allowing improved CTE performance of 0.99995 and 0.99999, respectively. Fortunately, today's CCDs can achieve a proportional transfer loss of less than 5×10^{-6} between pixels (CTE = 0.999995), and therefore in most CCD applications this loss mechanism can be neglected.

5.2. Fixed transfer loss

Our experience with all CCDs tested to date has shown that fixed transfer loss always occurs. Spurious potential pockets and bulk state traps are the main mechanisms responsible for this type of degradation in CTE performance.[7] We find that the spurious potential pocket is fairly common and generally limits CTE performance. Only the best of the CCDs are limited by bulk state trapping.

The spurious potential pocket is a characteristic that causes a fixed loss of charge due to improper potential well shape and/or depth. Spurious potential pockets may be found in every pixel for some CCDs (typically caused by a mask misalignment during the fabrication of the CCD), which has a disastrous effect on CTE performance. In other cases, spurious pockets are associated with single isolated pixels randomly found on the array, which causes charge spreading of the x-ray event in the form of a CTE tail. It is also common to experience spurious potential pockets at interface regions on the CCD array. A textbook example of this problem is demonstrated by the TI 3PCCD, where a spurious potential pocket is found in every column at the transfer interface that separates the imaging section from the horizontal transport register.[7] The effects of this problem on x-ray performance are demonstrated below using a computer simulation of this device.

The spurious potential pocket has been characterized in detail in order to analytically describe its behavior. We find that passing the charge packet from an x-ray event through a single spurious pocket will give rise to the following output signal:

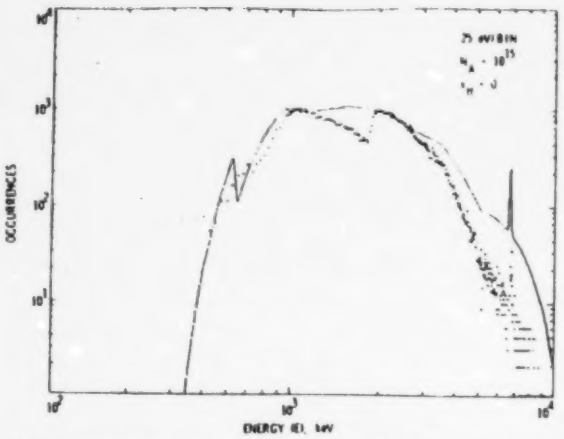

Fig. 14. Response of structure A to a synthetic astronomical spectrum. The input spectrum is that of the binary pulsar Her. X-1, transmitted through the AXAF telescope, and is shown as the solid line.[11] The discrete data points indicate the predicted CCD output accumulated in 20-eV bins.

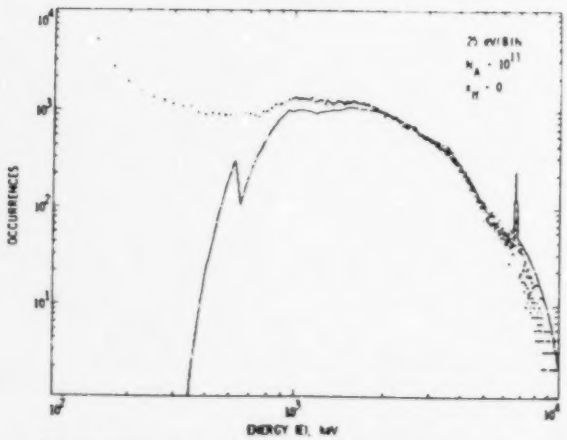

Fig. 15. Structure B presented in the manner of Fig. 14.

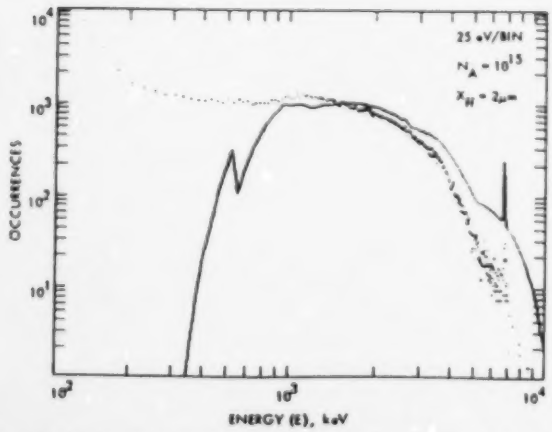

Fig. 16. Structure C presented in the manner of Figs. 14 and 15.

$$Q_1 \simeq Q_{p-s} - Q_\ell \,.$$

$$Q_n \simeq Q_1\left(\left\{1 - \exp\left[-\left(\frac{n-1}{\tau}\right)\right]\right\} - \left\{1 - \exp\left[-\left(\frac{n-2}{\tau}\right)\right]\right\}\right) \cdot \quad n = 2,3,4,\ldots \,; \tag{16}$$

$$Q_1 \simeq 0 \,.$$

$$Q_n \simeq Q_{p-s}\left(\left\{1 - \exp\left[-\left(\frac{n-1}{\tau}\right)\right]\right\} - \left\{1 - \exp\left[-\left(\frac{n-2}{\tau}\right)\right]\right\}\right) \cdot \quad n = 2,3,4,\ldots \,; \tag{17}$$

where Q_ℓ represents the loss due to the spurious potential pocket. Equation (16) is used to describe the CTE effects of a spurious pocket when the loss to the pocket is less than the charge of the x-ray event in the primary or adjacent pixel. Equation (17) is used when the loss is greater than the initial charge. The constant τ is given by[7]

$$\tau \simeq \tau_t \times \exp\left(\frac{-\Delta E}{kT}\right) \cdot \tag{18}$$

where τ_t is the transfer time through the spurious pocket, ΔE is the potential pocket depth, k is the Boltzmann constant, and T is the absolute temperature.

Figures 21 and 22 demonstrate the effects of fixed transfer loss due to spurious pockets using the equations above with the Monte Carlo simulation. In Fig. 21, we simulate the output response of the CCD to four x-ray lines spaced 250 eV apart under perfect CTE conditions. In Fig. 22 the same computation is performed except we assume that each x-ray event experiences a spurious potential pocket with a fixed loss Q_ℓ of 50 e^-. We also vary the fixed loss for each x-ray event by a sigma of $\sigma_\ell = 10\ e^-$.

The simulation in Fig. 22 represents the TI 3PCCD discussed above, which has a spurious potential pocket in each column that traps an average of 50 e^- of charge from each x-ray event ($T = 95°C$ and $\tau_t = 30$ ms). Comparing Figs. 21 and 22, we observe that the effects of only a 50 e^- fixed loss can dramatically degrade the x-ray performance of the CCD, especially for lower energy x rays. Note that the 250 eV line completely disappears into the 10 e^- noise skirt. Fortunately, the effects of the spurious pockets and bulk state trapping can be eliminated through use of a fat-zero charge. In the case of TI 3PCCD, a 100 e^- fat-zero is used to yield perfect CTE performance. However, the addition of this bias charge does add a shot noise component of 10 e^-, which adds in quadrature to the 10 e^- read noise floor, yielding a total noise floor of 14 e^-. This in turn degrades the energy resolution of the device.

6. EXPERIMENTAL DATA

Experimental data from many of our recent tests are reported elsewhere.[2,3,7,8] We summarize them only briefly here. The excellent capability of the CCD as an x-ray sensor is demonstrated in Fig. 23. The figure presents an x-ray histogram using an Fe^{55} source (5.9 keV) generated by a thinned fully depleted backside-illuminated CCD (TI 3PCCD). The simu-

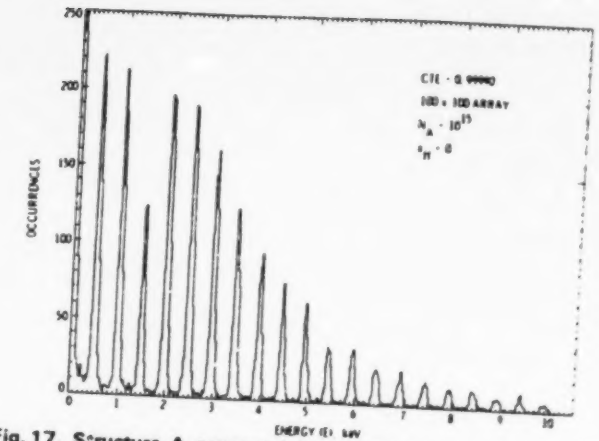

Fig. 17. Structure A presented for a 100×100 pixel CCD that includes in the simulation a proportional transfer loss in both the vertical and horizontal transfer directions. A CTE of 0.9999 is assumed.

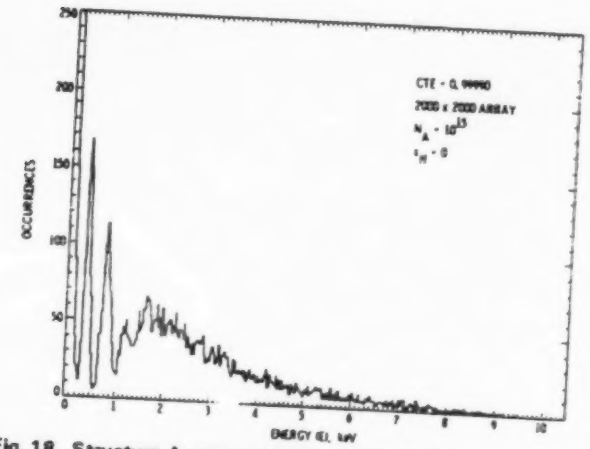

Fig. 18. Structure A presented for a 2000×2000 CCD using the same proportional transfer loss as Fig. 17.

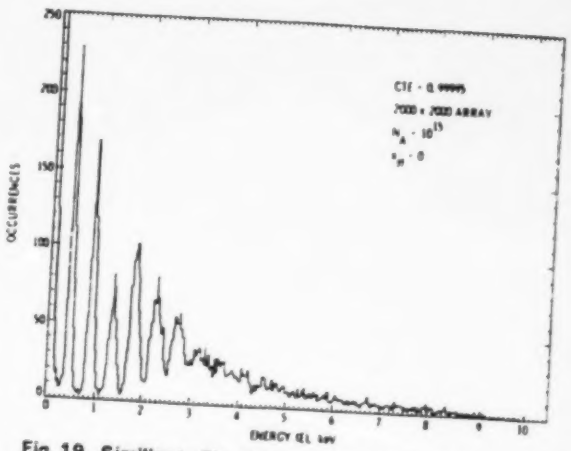

Fig. 19. Similar to Fig. 18 assuming a CTE of 0.99995.

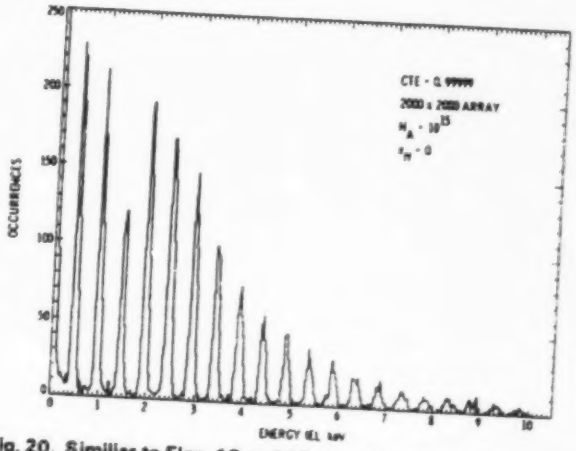

Fig. 20. Similar to Figs. 18 and 19 assuming a CTE of 0.99999.

lation that best fits this particular CCD is shown in Figs. 6, 10, and 14 for an impurity concentration of $N_A = 10^{13}$. At 5.9 keV, the simulation predicts that roughly 13% of the x-ray events should split, mainly due to the initial cloud diameter. Experimentally we find for the TI 3PCCD that 20% of the x-ray events split between two pixels with less than 1% splitting between three or more pixels. Again we assume that an event is split when 1% of the initial charge is lost from the primary pixel to an adjacent pixel. In the case of a 5.9-keV x-ray event, a 16 e^- loss is considered split. The difference in the number of split events between simulation and experiment has been attributed to the CCD channel stop regions, which have not been modeled in the simulation. Field analysis[3] has shown that field-free material exists for the TI 3PCCD and that increased charge splitting is expected. Future modeling of these regions might give insight into the magnitude of their effect on charge splitting.

Figure 24 is a histogram similar to Fig. 23 but incorporating more x-ray events. Here the x-ray histogram is assembled using only single pixel events (i.e., 20% of the events are rejected since they are split). Note the near-perfect separation of the Mn-K_α and Mn-K_β lines in addition to detection of both escape peaks and the silicon absorption peak. Finally, an Ag-L_α peak is discerned (Ag is present in the source) as well as the Mn-L_α lines. The partial event floor of this histogram is extremely small (<0.1%), indicating that virtually all the signal charge from each event is collected.

The effect of field-free material is more evident for the CCD that is not thinned. For example, Fig. 25 shows the response of a thick Texas Instruments frontside-illuminated virtual phase CCD fabricated with 15 μm, 100 $\Omega \cdot$ cm($N_A = 10^{14}$ cm^{-3}) epitaxial material. The device exhibits numerous split events since the depletion region extends no more than 10 μm, leaving at least 5 μm of field-free material between the epitaxial interface and depleted region. Here we find that 25% of the events are split between two pixels and 40% are split between three or more pixels. Also we find for this sensor numerous partial events that we believe are generated in the substrate below the epitaxial interface.[8]

7. CONCLUSIONS

CCDs offer tremendous potential as detectors for many x-ray applications. However, it is clear that trade-offs must be made between sensitivity and charge collection performance in choosing the optimum CCD for each specific application. At

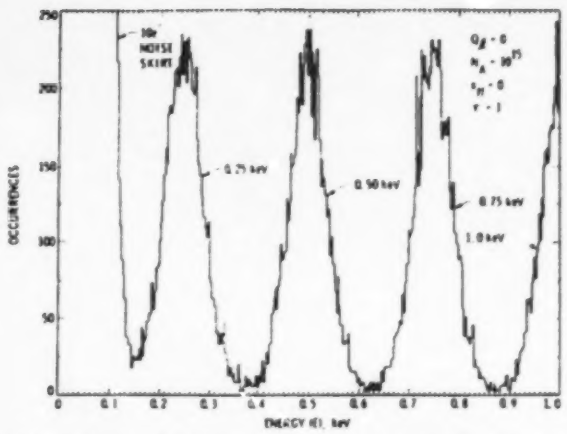

Fig. 21. Structure A simulated without charge transfer loss, showing four low energy x-ray lines (250, 500, 750, and 1 keV) and a 10 e^- read noise skirt. In this simulation we assume the CCD is uniformly illuminated with 1 x-ray interaction per 1000 pixels.

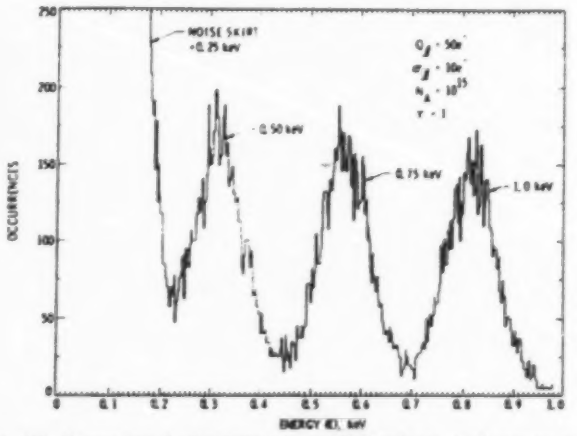

Fig. 22. Structure A simulated for a CCD where each x-ray event experiences a fixed transfer loss of Q_t = 50 e^- with a variation in loss of σ_t = 10 e^-. The simulation best describes the TI 3PCCD, which has spurious potential pockets located at the interface between the imaging array and horizontal transport register.

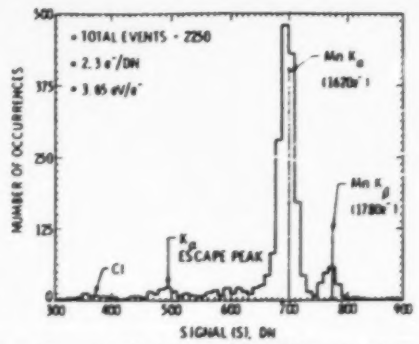

Fig. 23. Experimental histogram of 2250 x-ray photons from an Fe^{55} source taken with the backside-illuminated TI 3PCCD using a fat-zero charge of 110 e^-.

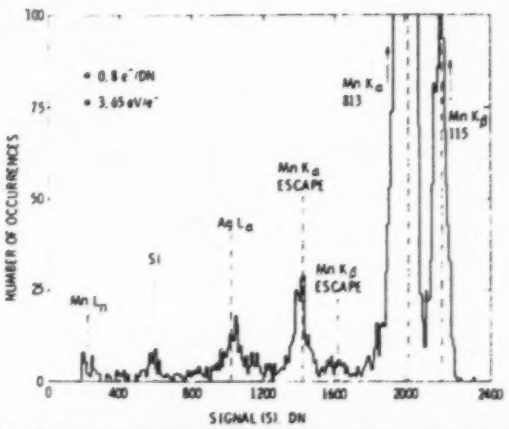

Fig. 24. Experimental histogram of single pixel events for an Fe^{55} x-ray source using the backside-illuminated TI 3PCCD demonstrating a very low partial event floor.

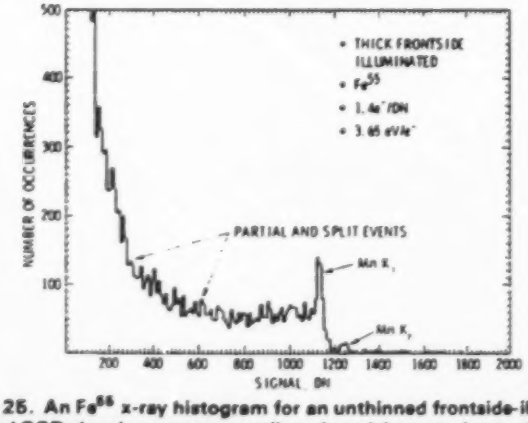

Fig. 25. An Fe^{55} x-ray histogram for an unthinned frontside-illuminated CCD showing numerous split and partial events due to charge diffusion in field-free material.

high energy, front- and backside-illuminated devices perform equally well, provided they are relatively thick ($\simeq$ 30 μm), fully depleted, and free of backside recombination layers. At low energy, one must choose between the greater sensitivity of a backside-illuminated device and the greater charge collection efficiency of a frontside-illuminated device. For ACIS, this trade-off tends to favor the thinned frontside-illuminated CCD because the UV/visible blocking filters required will substantially reduce the sensitivity gain offered by backside-illuminated structures. The challenge now is to incorporate these desired x-ray features in fabricated CCDs without compromising those other CCD characteristics (charge transfer efficiency and readout noise) on which x-ray performance critically depends. Limited industrial capacity is devoted to the production of high performance scientific CCDs. Therefore, meeting this challenge will not be easy.

8. ACKNOWLEDGMENTS

The authors would like to thank Steve Prado for providing Eqs. (3), (4), and (5) and x-ray spectra for Her. X-1. Special thanks to Morley Blouke, Jim McCarthy, Mark Wadsworth, Jim Morrison, George Ricker, and Larry Simmons for many rewarding conversations about which we write. The research described was carried out by the Jet Propulsion Laboratory, California Institute of Technology, under contract with the National Aeronautics and Space Administration.

9. REFERENCES

1. G. Garmire et al., "The AXAF CCD imaging spectrometer," in *X-Ray Instrumentation in Astronomy*, J. L. Culhane, ed., Proc. SPIE 597, 261-266 (1986).
2. R. Stern, K. Liewer, and J. Janesick, "Evaluation of a virtual phase charge-coupled device as an imaging x-ray spectrometer," Rev. Sci. Instrum. 54(2), 198-205 (1983).
3. J. Janesick, T. Elliott, H. Marsh, S. Collins, J. McCarthy, and M. M. Blouke, "Potential of CCDs for UV and x-ray plasma diagnostics," Rev. Sci. Instrum. 56(5), 796-801 (1985).
4. J. Janesick, T. Elliott, J. McCarthy, H. Marsh, S. A. Collins, and M. Blouke, "Present and future CCDs for UV and x-ray scientific measurements," IEEE Trans. Nucl. Sci. NS-32(1), 409-416 (1985).
5. J. Janesick, J. Hynecek, and M. M. Blouke, "Virtual phase imager for Galileo," in *Solid State Imagers for Astronomy*, J. C. Geary and D. W. Latham, eds., Proc. SPIE 290, 163-173 (1981).
6. M. M. Blouke, J. Janesick, J. E. Hall, M. W. Cowens, and P. May, "800X800 charge-coupled device image sensor," Opt. Eng. 22(5), 607-614 (1983).
7. J. R. Janesick, T. Elliott, S. Collins, H. Marsh, M. Blouke, and J. Freeman, "The future scientific CCD," in *State-of-the-Art Imaging Arrays and Their Applications*, K. N. Prettyjohns, ed., Proc. SPIE 501, 2-31 (1984).
8. J. Janesick, K. Klaasen, and T. Elliott, "CCD charge collection efficiency and the photon transfer technique," in *Solid State Imaging Arrays*, K. N. Prettyjohns and E. L. Dereniak, eds., Proc. SPIE 570, 7-19 (1985).
9. J. Janesick, T. Elliott, T. Daud, and J. McCarthy, "Backside charging of the CCD," in *Solid State Imaging Arrays*, K. N. Prettyjohns and E. L. Dereniak, eds., Proc. SPIE 570, 46-79 (1985).
10. J. Janesick, T. Elliott, T. Daud, and D. Campbell, "The CCD flash gate," in *Instrumentation in Astronomy VI*, D. L. Crawford, ed., Proc. SPIE 627, 542-582 (1986).
11. J. Bresse, "Electron beam induced current in silicon planar p-n junctions: physical model of carrier generation. Determination of some physical parameters in silicon," in *Scanning Electron Microscopy*, 5th Annual Symposium (Chicago), IIT Research Institute and National Institute of General Medical Science (1972).
12. R. Brodersen, D. Buss, and T. Tasch, "Experimental characterization of transfer efficiency in charge coupled devices," IEEE Trans. Electron Devices ED-22, (1975).

James R. Janesick was born in Orange, Calif., in 1947. He received his master's degree in electronic engineering from the University of California at Irvine, majoring in lasers and masers. Since January 1973 he has been working at the Jet Propulsion Laboratory, California Institute of Technology, developing charge-coupled devices for the wide field/planetary Hubble Space Telescope camera, the Galileo solid-state imaging camera, and other NASA space imaging systems. He is author of 15 papers on the subject of CCDs, has contributed to several NASA tech briefs, and holds three patents on various CCD innovations. He received the Exceptional Engineering Achievement medal from NASA in 1982 and a NASA Achievement Award in 1986. He is currently involved in the development of narrow band-gap monolithic CCD sensors for infrared and x-ray imaging space instruments.

Stythe T. Elliott was born in Van Nuys, Calif., and received his BA degree in geography from the California State University at Northridge. He joined the Jet Propulsion Laboratory in 1979 and is presently developing charge-coupled devices for NASA space imaging systems, including the wide field/planetary Hubble Space Telescope camera. He received a NASA Achievement Award in 1986.

Stewart A. Collins received his BS degree from Principia College in 1969 and has been employed by the Jet Propulsion Laboratory since that time. He is supervisor of the JPL Imaging Systems Section's Advanced Development Group, which is responsible for the development of imaging detectors for various NASA space imaging systems.

Taher Daud received his BS degree in electrical engineering from the University of Jabalpur, India, and MS and Ph.D. degrees in solid-state electronics in 1976 and 1979 from the University of California, Los Angeles. He joined the Jet Propulsion Laboratory in 1976 and worked on the development of high efficiency solar cell and ribbon-silicon technology for the Flat-Plate Solar Array Project until 1985. He has also been involved in the development of a variety of semiconductor devices, including silicon-compatible modulation-doped infrared sensors. Presently, he is working on the CCD program to develop a theoretical understanding of backside-illuminated UV-sensitive sensors.

Dave Campbell received his BS degree in chemistry from the State University of New York at Binghamton and later attended Rensselaer Polytechnic Institute in Troy, N.Y., where he completed an MS degree in materials engineering in 1984. Since 1985 he has been with the Imaging Systems Section's Advanced Development Group at JPL, doing device modeling and thin-film coatings research.

Gordon P. Garmire was born in Portland, Ore., in 1937 and studied at Harvard University, where he received the AB degree in 1959. He then received his Ph.D. in physics in 1962 from MIT, where he continued as an assistant and then associate professor until 1967. In 1966 he joined the faculty at Caltech, where he was appointed a professor of physics in 1972. In 1980 he joined the astronomy faculty at The Pennsylvania State University and was appointed an Evan Pugh Professor in 1985. Dr. Garmire was a member of the MIT team that discovered high energy cosine gamma rays from our galaxy. He was co-principal investigator on NASA's first High Energy Astronomy Observatory and is an instrument principal investigator on the Advanced X-ray Astrophysics Facility planned by NASA for a launch in the mid 1990s. In 1974 Dr. Garmire was a Guggenheim Fellow and held a Senior Hays Fulbright scholarship. He received NASA's Exceptional Scientific Achievement award in 1978. He was chairman of the High Energy Division of the American Astronomical Society in 1985.